4. Pressure Measurement Systems

Measurements of the steady pressure in a fluid flow may be required to determine other thermodynamic properties, to determine forces on a body due to the pressure distribution over it, or in order to determine the dynamic head and flow velocity (for further details on the latter see Sect. 5.1. Pressure is a scalar representation of molecular activity, a measure of the nondirectional molecular motions. Thus it must, by definition, be measured by a device at rest relative to the flow. Whilst the common practice in the fluid mechanics community is to denote the pressure as *static* (as opposed to the coordinate-dependent *total pressure*, Sect. 3.1), this terminology introduces a fundamental redundancy.

In practice, pressure is commonly measured both at walls and in the freestream using the types of measurement device shown in Fig. 4.1 connected to a transducer of suitable sensitivity and range. The orifice of a small wall tapping represents a simple way to obtain the pressure impressed on the wall by the external flow. So-called static pressure tubes approximate the local fluid pressure in the freestream if the disturbance presented to the flow can either be accounted for or is not large to begin with. However this can only ever be strictly true for steady laminar flow due to the normal velocity component introduced when a flow becomes turbulent. Measurement of freestream pressure is one of the hardest challenges in fluid mechanics.

This chapter addresses measurement of pressure using wall tappings (Sect. 4.1) and static pressure tubes (Sect. 4.2), and especially errors due to the intrusive flow presence of real, finite-sized devices and calibrations to correct for these. *Bryer* and *Pankhurst* [4.1] and *Chue* [4.2] provided seminal monographs on the general topic of pressure probes in 1971 and 1975, respectively, which give detailed descriptions of measurement devices, coverage of the background to the various corrections and a survey of older data. The topic is covered here more concisely, with a view to practical use by the engineer, and with reference to modern literature. The reader is referred to *Bryer* and *Pankhurst* [4.1] and *Chue* [4.2] for further details on most sections.

In more recent years a further method for obtaining pressure on the surface of a wind tunnel model has been developed, based on pressure sensitive paints (PSP). The introduction of PSP provides a method to measure the pressure on the surface of a model directly without the transducers and tubing associated with conventional means. A paint, the luminescence of which is dependent on air pressure, is applied to the surface of a wind tunnel model and the pressure distribution is obtained from the images produced by proper illumination. In Sect. 4.4 the basics of PSP are discussed and further subsections address in detail different paints, paint application procedures, imaging systems and image processing. In discussing the achievable accuracy of PSP techniques, both the spatial and temporal resolution is examined. The thermal sensitivity of the paint dye is introduced and this is closely linked to temperature-sensitive paints (TSP), as discussed in Chap. 7, Sect. 7.4.

4.1 **Measurement of Pressure with Wall Tappings** 180
4.1.1 Cavity Shape, Connection and Alignment 181
4.1.2 Finite-Area Effects 181
4.1.3 Effect of Compressibility 182
4.1.4 Effect of Finite Depth 183
4.1.5 Condition of the Orifice Edge 184
4.1.6 Correction for Distance from Measuring Point 184

4.2 **Measurement of Pressure with Static Tubes** 185
4.2.1 Effect of Geometry 185
4.2.2 Effect of Hole Location 186
4.2.3 Directional Sensitivity 186
4.2.4 Effect of Turbulence 186

4.3 Hardware and Other Considerations 187
4.4 Pressure-Sensitive Paint (PSP) 188
4.4.1 Basics of PSP 188
4.4.2 Paints 190
4.4.3 Imaging Systems 200
4.4.4 Processing 204
4.4.5 Applications 206
4.4.6 Concluding Remarks 208
References 209

4.1 Measurement of Pressure with Wall Tappings

A wall tapping, or piezometer, is a simple means of obtaining pressure at the wall, p_w, in a wall-bounded flow, but one that requires some subtlety in many flows. For example, accurate determination of the pressure distribution on a scale model in a small-cross-section high-Mach-number wind tunnel may be complicated by changes in the flow field due to the diameter of the tappings (dictated by manufacturing or response time constraints, Sect. 4.1.4), which may be large compared to the boundary-layer thickness (which changes with the streamwise location).

The finite size of tappings that can be reliably and smoothly manufactured may be sufficiently large to induce an error in the measured pressure, such that $p_{wm} = p_w + \Delta p_w$. Dimensional analysis shows that, for a pressure tapping of a given geometry in a zero-pressure-gradient flow (or where the tapping diameter is small compared with the scale of pressure variation), Δp nondimensionalised with the wall shear stress τ_w is a function of the following variables:

$$\Pi = \frac{\Delta p}{\tau_w} = f\left(\frac{d_s u_\tau}{\nu}, \frac{d_s}{D}, M, \frac{l_s}{d_s}, \frac{d_c}{d_s}, \frac{\epsilon}{d_s}\right) \quad (4.1)$$

and, of course, the (laminar or turbulent) condition of the wall-bounded flow. Here d_s is the tapping (orifice) diameter, $u_\tau = \sqrt{\tau_w/\rho}$ is the friction velocity, D is the flow lengthscale, M is the Mach number (the ratio of local velocity to the local speed of sound), l_s is the depth of the orifice, d_c is the diameter of the cavity behind the orifice, ϵ is the root-mean-square height of burrs on the edge of the tapping orifice, ρ is the fluid density and ν is the kinematic viscosity (Fig. 4.1a). The true pressure at the wall, p_w, is then given by

$$p_w = p_{mw} - \Pi \tau_w \,. \quad (4.2)$$

The complexity of the flow local to the tapping means that analytical or numerical solutions for the pressure error are at present available only for very low Reynolds numbers and/or two-dimensional geometries, e.g. [4.3]. The majority of the experimental data is for a turbulent flow over the orifice, and comparisons of experiments reveal significant scatter between results, probably due to the difficult nature of the experiments (a pressure error that is of the same order as the experimental uncertainty) and extrapolation of the *true* pressure for quantification of the error. In what follows, we tackle the effect of each of the nondimensional parameters in (4.1) on the measurement error.

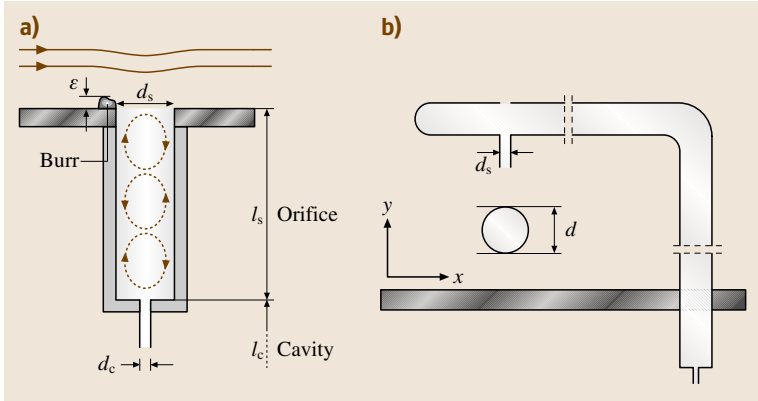

Fig. 4.1a,b Determination of steady pressure: **(a)** wall tapping; **(b)** static tube

4.1.1 Cavity Shape, Connection and Alignment

First we consider the effect of orifice shape. While the traditional geometry employed for measurement of pressure at the wall is the straight-edged, circular cylinder drilled perpendicular to the plane of the wall (as in Fig. 4.1a), researchers have experimented with several other geometries, including slot-type (noncircular) [4.2], angled [4.4] and radiused or chamfered-edge circular tappings ([4.4], Sect. 4.1.5). In addition, various connector geometries from the tapping to the transducer have been designed, dictated by experimental constraints, manufacturing (i. e. drilling) techniques and even with the goal of reducing the pressure error. The efforts of *Allen* and *Hooper* [4.5] in seeking to define a commercial standard for tapping geometry through the investigation of geometries including recessed, conical, countersunk and protruding orifice tubes were essentially inconclusive, although they did yield several useful scaling trends.

The difference between the pressure measured by cylindrical and slot-type tappings at supersonic speeds is of the order of $\pm$ 1% (Douglas Aircraft company tests reported by *Chue* [4.2]), with implications for appropriate correction of measurements from tappings that are drilled out-of-round.

The directional sensitivity of tappings and effect of alignment of the tapping with the wall normal direction was investigated by *Rayle* [4.4], who found a zero error when the tapping centreline was angled 30° downstream with respect to the outward wall normal, increasing/decreasing as the centreline was rotated upstream/downstream, respectively.

The analysis of *Ducruet* and *Dyment* [4.6] identifies an effect of radius of curvature r_b of the wall containing the orifice, of obvious importance when $d/r_b \sim \mathcal{O}(1)$. While this suggests that there will be a difference in the errors induced by tappings in pipe, flat plate boundary layers/channels and bodies of revolution, etc., this effect has not been identified in the majority of the experimental literature and results from flat and curved surfaces have been used together in an attempt to obtain general scaling laws.

The below-surface geometry of the tapping (i. e. the cavity geometry and ratio d_s/d_c) will also have an effect. Chue suggests that differences between the experimental results of *Livesey* et al. [4.7] (a *pinhole* design, with $d_s/d_c = 1/14$ and $l_s \ll l_c$) and *Shaw* [4.8] (cylindrical tappings with $d_s/d_c = 1/2$ and l_s large) must lie in the wall fittings, all other parameters being equal. This is discussed further in Sect. 4.1.4.

In summary, while the current knowledge concerning straight-edged, cylindrical tappings will be reviewed here, use of other geometries will most likely require in situ calibration over the expected range of flow conditions to obtain wall pressure measurements with high confidence.

4.1.2 Finite-Area Effects

Given a deep tapping with smooth edges, the finite size (diameter) of the tapping causes local curvature of the streamlines and a complicated system of vortices within the cavity (and potentially a stagnation point on the downstream wall), as sketched in Fig. 4.1a and observed by *Miyadzu* [4.9] and *Ray* [4.10]. The effect of a finite tapping diameter on the measured static pressure is expressed in the dependence of the pressure error on both $d_s^+ = d_s u_\tau/\nu$ and d_s/D, the ratios of tapping diameter to viscous scale and flow lengthscale, respectively:

$$\Pi = f\left(d_s^+, \frac{d_s}{D}\right) . \tag{4.3}$$

Measurements of Π are extremely difficult to make due to the small magnitude of the pressure differences, the sensitivity to manufacturing tolerances, the need to isolate only either d_s^+ or d_s/D (especially hard in boundary layers where both the friction velocity and the dominant lengthscale, the displacement thickness δ^*, change with streamwise location) and the difficulty of establishing the *zero-error* condition (by extrapolation [4.8] or use of a flush surface pressure transducer [4.11]), where $\Pi \to 0$ as $d^+ \to 0$. Studies include those by *Miyadzu* [4.9], *Ray* [4.10], *Franklin* and *Wallace* [4.11] and *Ducruet* and *Dyment* [4.6] on the static hole error in a plane surface (i.e. beneath a flat plate turbulent boundary layer or in channel flow), *Fuhrmann* [4.12] in an axisymmetric turbulent boundary layer and *Allen* and *Hooper* [4.5], *Rayle* [4.4], *Shaw* [4.8] and *Livesey* et al. [4.7] in pipes. However the results are quite scattered due to variations in the exact geometries of the tappings under test.

For tappings that are *small* with respect to the flow lengthscale D, the results of *Shaw* [4.8], obtained in a pipe for $0.008 < d_s/D < 0.1$, $25 < d_s^+ < 800$ and $1.5 \le l_s/d_s \le 6$ ($M < 0.2$) had been used as the standard for the variation of pressure error with diameter for deep holes. However more recently *McKeon* and *Smits* [4.13] also explored the pressure error in pipe flow, extending the range of Reynolds numbers by changing d_s^+ without making d_s/D large ($0.0020 \le d_s/D \le 0.0184$,

$d_s^+ \leq 8000$) with $M \leq 0.07$ and $l_s/d_s = 4$ with effectively infinite connection. They found that *Shaw*'s [4.8] results masked the dependence of the error on d_s/D.

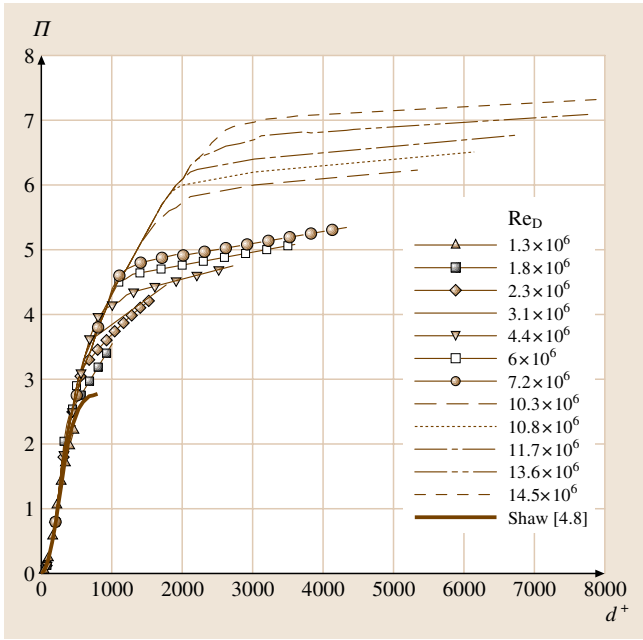

Fig. 4.2 Effect of hole size on pressure error, Π, in pipe flow (After *McKeon* and *Smits* [4.13]). Each curve corresponds to the error found from a set of wall tappings with $0.002 \leq d_s/D < 0.02$ at one pipe Reynolds number, i. e., the variation in local Reynolds number d_s^+, is achieved at each pipe Reynolds number by changing d_s/D

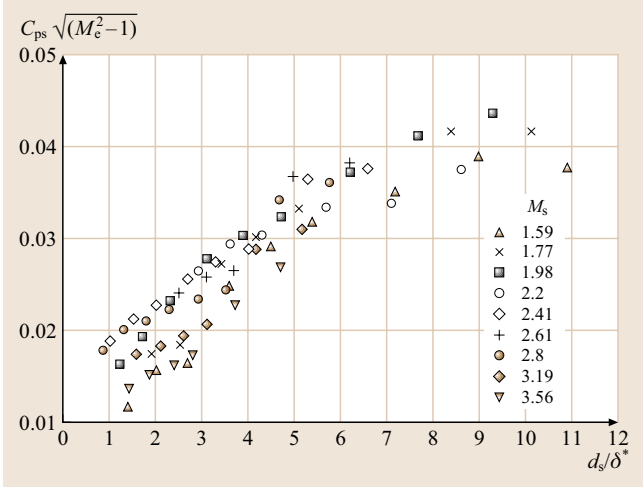

Fig. 4.3 Effect of compressibility on pressure corrections for large holes (After *Rainbird* [4.14])

Curve fits to their data are replicated in Fig. 4.2, showing the effect of increasing the pipe Reynolds number on the pressure error for the same set of different diameter tappings. While Π is a function of tapping Reynolds number alone alone for low d_s^+, the influence of d_s/D becomes increasingly important, even for tappings with small diameters. At the same d_s^+, the error for a small tapping exceeds that for a large one (although note that the pipe Reynolds number will be much larger for the small tapping).

The intuitively simple proposal of Livesey et al. to relate the pressure error to observed streamline deflection through an integral of the dynamic pressure at a distance proportional to d_s from the surface gives a curve similar to those in Fig. 4.2 (but not exactly the same).

For large tappings and high tapping Reynolds number, the data indicate [4.13, 14] that the pressure error tends to a function of d_s/D alone, hence plots of the pressure coefficient $C_{ps} = \Delta p/(1/2\rho U^2)$ versus d_s/D would be more appropriate. This has been addressed in the compressible, high-Reynolds-number regime, where experiments have often been performed with d_s/D orders of magnitude larger than in the incompressible case because of limitations on manufacturing smooth small orifice tappings and thin boundary layers.

In summary, the error introduced into the measurement of pressure at the wall by a tapping of finite diameter in turbulent flow is positive for deep holes and increases with the ratio of the hole diameter to the viscous scale, d_s^+ (for a given tapping diameter d_s/D), but decreases as the ratio to the flow lengthscale, d_s/D, increases (for a given d_s^+). Of course the error will be averaged out in the measurement of pressure gradient in steady internal flows since the flow lengthscale does not change; however for boundary-layer pressure gradients the effect may be significant. Note that Rainbird suggests that the error, Π, for large holes in laminar flow does not tend to a high-Reynolds-number asymptote and can become very large, $\mathcal{O}(50)$.

In a flow with a rapid spatial variation of pressure, there will be an additional effect of spatial averaging of the pressure measured by a tapping that is large compared with the lengthscale of pressure variation.

4.1.3 Effect of Compressibility

The effect of compressibility has not often been isolated experimentally, particularly due to the competing effects of putting small tapping diameters into small models while requiring rapid response times due to generally short run times in higher-Mach-number facilities.

Rainbird performed measurements with large tappings ($0.7 \le d_s/\delta^* \le 10.9$) normal to the axis of a cone under a zero-pressure-gradient boundary layer at Mach numbers external to the boundary layer $1.59 \le M_e \le 3.56$. When plotted in the form $C_{ps}/\sqrt{M_e^2-1}$ versus d_s/δ^* for high Reynolds numbers only ($d_w^+ > 1000$ based on wall conditions), as in Fig. 4.3, the data demonstrate a general trend of increasing error with decreasing Mach number and increasing d_s/δ^* (at least for the smaller tapppings). *Rainbird* [4.14] proposed that for $d_s/\delta^* > 10$ approximately, the calibration coefficient is given by

$$C_{ps} \approx \frac{0.04}{\sqrt{M_e^2-1}} \,. \tag{4.4}$$

Note that *Plentovich* [4.15] recorded the generation of Mach waves by finite-sized tappings on a National Advisory Committee for Aeronautics (NACA) 65_1 613 airfoil at $0.6 \le M_\infty \le 0.8$ and high chord Reynolds number (also inconclusive results concerning the efficiency of fitting a porous metal plug in the tapping flush with the orifice in reducing the measurement error). Finally, *Ducruet* [4.16] has suggested that the effect of Mach number is more important for laminar than turbulent boundary layers.

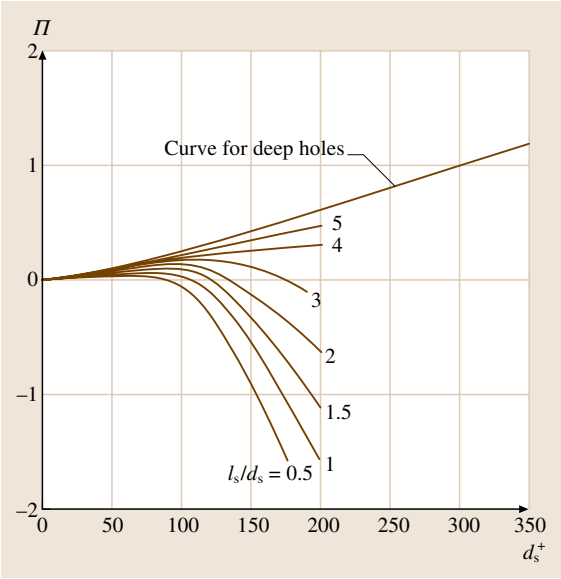

Fig. 4.4 Variation of pressure error Π with relative tapping depth l_s/d_s for pinhole-type tappings with $d_c = 14d_s$ (After *Livesey* [4.7])

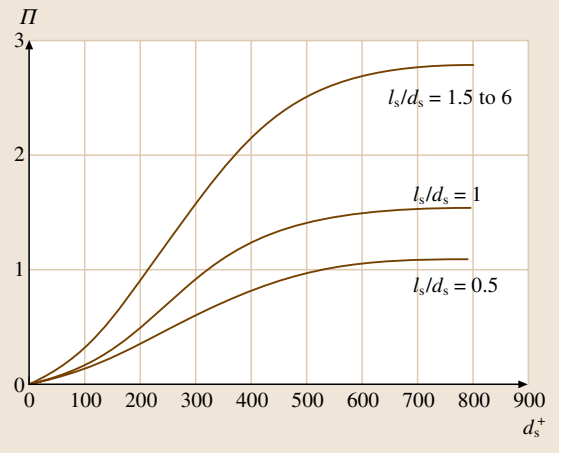

Fig. 4.5 Variation of pressure error Π with relative tapping depth l_s/d_s for narrow tappings with $d_c = 2d_s$ (After *Shaw* [4.8])

4.1.4 Effect of Finite Depth

The depth of the tapping cavity l_s is defined here as the distance between the plane of the wall and either the cavity behind the orifice or the connection to the transducer, with diameter d_c and depth l_c, as in Fig. 4.1a. This parameter impacts on the extent of the system of eddies that is set up within the tapping and has been shown to affect the magnitude of the pressure error in a complex fashion (that also involves the relative cavity width with respect to the orifice, d_c/d_s). As such, several authors have sought to eliminate the depth from the problem by defining a minimum *deep* tapping l_s/d_s ratio beyond which the error ceases to change. A consensus appears to be $l_s/d_s \approx 2$, e.g. [4.5, 8, 9].

For shallower tappings, *Ray* [4.10] investigated tappings with $0.1 \le l_s/d_s \le 1.75$ and varying connection diameter d_c in a low-aspect-ratio duct and proposed that the error could be represented as follows for $1.7 < d_s^+ < 31.6$:

$$\Pi = f\left(\frac{l_s}{d_s}\right)\sqrt{d_s^+} \tag{4.5}$$

with

$$\begin{aligned} f\left(\frac{l_s}{d_s}\right) &= 0.25 \quad \text{for} \quad l_s/d_s = 1.75 \,, \\ &= 0.54 \quad \text{for} \quad l_s/d_s = 0.1 \,. \end{aligned} \tag{4.6}$$

Livesey et al. found a similar trend of increasing error with hole depth for tappings with a large d_c, and a deep hole limit of $l_s/d_s \approx 7.5$. For this d_c configuration and low l_s/d_s, the sign of the error changes with increasing d^+ (Fig. 4.4), as also noted by *Miyadzu* [4.9] for

$l_s/d_s = 0.4$. Seeking to eliminate the error, Livesey et al. proposed that tappings with $l_s/d_s = 2$ and $d_c/d_s = 14$ have $\Pi \sim 0$ for $0 < d_s^+ < 300$, at least for their experimental setup.

Shaw's investigation also included shallower tappings, in the range $0.5 \le l_s/d_s \le 6$ (with $d_c/d_s = 2$). He found that the pressure error was independent of the depth-to-diameter ratio for $l_s/d_s > 1.5$, but that the error steadily decreased for shallower tappings. The errors for tappings with $d_s^+ < 750$ and depth $l_s/d_s = 0.5$, 1 and ≥ 1.5 are shown in Fig. 4.5 (although note that the effect of d_s/D detailed in Sect. 4.2.2 may also apply to these results).

4.1.5 Condition of the Orifice Edge

Two aspects of the condition of the orifice edge have been shown to affect the pressure error by altering the flow field in and around the tapping: the size of any burrs remaining after drilling [4.5, 8] and the magnitude of the radius on the edge of the hole (either imposed or caused by drilling, sanding or polishing [4.4, 5, 8]). A smooth upstream surface approaching the tapping is assumed.

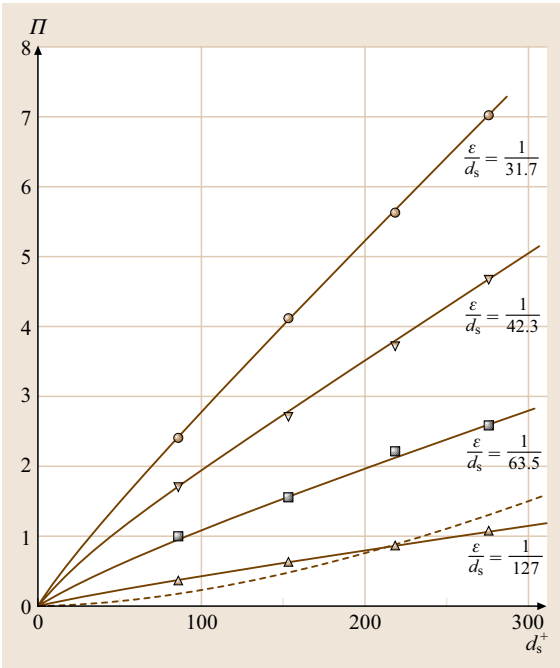

Fig. 4.6 The effect of the condition of the tapping orifice edge: the variation of the pressure error Π with relative burr height ϵ/d_s (After *Shaw* [4.8]). The dashed line is the small-tapping, zero-burr error

The effects of the form of the orifice edge on the pressure error can be summarised [4.4] as an increasing positive error with increasing edge radius and increasing negative error with increasing depth of chamfer (for a constant chamfer angle of 82°). Errors of up to −1% relative to the *dynamic* pressure measured in the straight-edged case have been observed (see also the pictorial summary by *Chue* [4.2]). *Allen* and *Hooper* [4.5] confirm this trend with edge radius and suggest that a radius of $d_s/4$ or smaller gives no detectable error. These authors also found errors of up to −0.4% of the mean velocity head for burrs hanging over/into the tapping (i. e. not protruding into the flow). Large negative errors were also observed for orifice tubes that protruded into the flow, increasing with the distance of protuberance from the pipe wall.

Shaw investigated the effect of burr heights in the range $1.57 \times 10^{-4} < \epsilon/d_s \le 3.4 \times 10^{-2}$ on deep tappings ($l_s/d_s = 4$), with $d_s/D = 0.03175$ by varying the feed rate of the drill while maintaining the same drill speed. His results, shown here in Fig. 4.6, demonstrate that the burr height can cause an error that exceeds the one due to due to finite area for small holes (a maximum value of $\Pi \approx 8$ was observed for the largest burr at the highest $d_s^+ \approx 275$, but the error appears to increase linearly with d_s^+), and hence extreme care must be taken with the drilling process. Note also that a large speck of dust resting on the edge of a tapping could cause a similar effect, hence there is reason to clean out tappings before making sensitive measurements. Several authors have discussed the best method to produce small tappings without burrs or radiused edges (or out-of-round, Sect. 4.1.1). *Franklin* and *Wallace* [4.11] experimented with drilling, lapping and reaming techniques for the orifice and polishing for the surrounding surface, settling on a complicated method that used tapered plugs to fill the hole and grinding to take off any burrs and finish the surface (these plugs subsequently reamed the tappings on removal). A Talysurf optical profiler was used to inspect the orifice edges. *Zagarola* [4.17] used a 32 *times* optical level to inspect orifice edges holes after the surrounding pipe surface has been honed and polished.

Figure 4.7a,b show magnifications of two tappings from the study of *McKeon* and *Smits* [4.13]. These were drilled from the polished measurement surface inwards, thus reducing the expected level of burring, however the tapping in (a) was discarded due to the obvious burring ($\epsilon/d_s = 0.63 \times 10^{-3}$) although the error due to the burring was estimated to be negligible, while (b) was accepted and used in the experiments.

4.1.6 Correction for Distance from Measuring Point

Obtaining the pressure in the internal part of a turbulent flow from a measurement at the wall requires correction for the difference between local and wall pressure introduced by turbulent fluctuations. For boundary layers at high Reynolds number with thickness δ,

$$\frac{p_\mathrm{w}-p}{\tau_\mathrm{w}} = \frac{\overline{v'^2}}{u_\tau^2} + \frac{1}{u_\tau^2}\int_0^y \left(U\frac{\partial V}{\partial x} + V\frac{\partial V}{\partial y}\right) \mathrm{d}y \,, \quad (4.7)$$

which will depend on the degree of spatial variation of the flow (and where is has been assumed that the streamwise gradient of Reynolds shear stress $\partial\overline{u'v'}/\partial x$ is negligibly small). In pipe flow with radius R,

$$\frac{p_\mathrm{w}-p}{\tau_\mathrm{w}} = \frac{\overline{v'^2}}{u_\tau^2} + \frac{1}{u_\tau^2}\int_r^R \left(\frac{\overline{w'^2}-\overline{v'^2}}{r}\right) \mathrm{d}r \,. \quad (4.8)$$

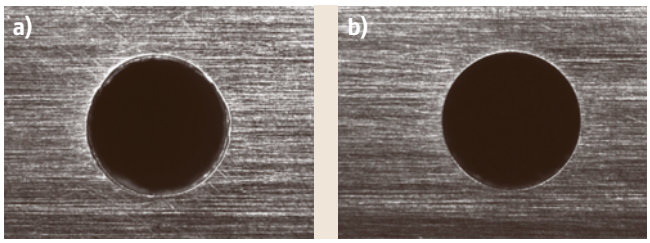

Fig. 4.7a,b Magnified images of wall tapping with $d_\mathrm{s} = 2.381$ mm. **(a)** Rejected due to burring ($\epsilon/d_\mathrm{s} = 0.63\times10^{-3}$) and **(b)** Accepted (After *McKeon* and *Smits* [4.13])

This latter pressure gradient has been measured indirectly by hot-wire anemometry (*Sandborn* [4.18]) and directly by static pressure tube (*Patterson* et al. [4.19]) for low to intermediate pipe Reynolds numbers. These measurements both found that the integral term on the right in (4.8) is negligible, and that the pressure difference $(p_\mathrm{w}-p)/\tau_\mathrm{w} \approx 1$ away from the wall and $(p_\mathrm{w}-p)/\tau_\mathrm{w} \to 0$ near the wall.

4.2 Measurement of Pressure with Static Tubes

A static tube such as that shown in Fig. 4.1b may be used to obtain the freestream pressure. This is a hard measurement to make, since strictly the probe should be at rest relative to the flow in order to measure the scalar quantity that is local pressure. In practice, rather than using a flying probe (with an unknown, complex trajectory in turbulent flow), a slender tube is aligned parallel to the incoming flow to minimise disturbance to the flow and the pressure is measured by several tappings in the same radial plane (to avoid the effect of local pressure gradients) downstream of the nose geometry. The measurement location is removed from both the probe tip and probe stem, and will be a point at which the surface pressure equals, or can be related by calibration to the undisturbed freestream value. Recall the pressure coefficient

$$C_\mathrm{ps} = \frac{p_\mathrm{m}-p}{\frac{1}{2}\rho U^2} \quad (4.9)$$

to account for the difference between the measured pressure and the true pressure at the measurement location. *Chue* [4.2] notes that the pressure measured by static tubes is essentially independent of Reynolds number in the range $3000 \le \mathrm{Re_d} \le 53\,000$, such that for most applications in which a static tube would be employed viscosity does not influence the reading.

Many of the results from the section on wall tappings carry over to errors introduced by the orifices in a static tube (which will be large compared with the boundary layer developing on the probe), but some additional effects should be considered. Note that, although much experimental work has been performed on Pitot-static probes (Sect. 5.1.3), negligible mutual interference between the measurements of total head and (static) pressure [4.1] means that some results can be applied equally well to static tubes.

Standard tip shapes include ellipsoidal and hemispherical designs for subsonic measurements. While cylindrical probes with rounded tips will primarily be considered here, other static pressure probes include a short-head design (where the static pressure holes are located at the downstream position corresponding exactly to the undisturbed static pressure), a spherical form, a static wedge and the static disc (which has the advantage of being largely insensitive to flow direction in the plane of the disc, but has been shown to demonstrate large variations in calibration function with Reynolds number and a nonlinear yaw calibration that should preclude its use in turbulent flow [4.20]).

4.2.1 Effect of Geometry

In general, probes that resemble a body of revolution with a rounded nose are used for subsonic flow, while an ogival or conical section may be preferable for supersonic flow. The latter design performs better by keeping the bow shock attached to the probe and minimising the disturbance to the flow. The static pressure is obtained from shock tables.

As the freestream Mach number approaches unity, the probe geometry will dictate the development of local shocks in the region of flow acceleration around the probe tip. With increasing Mach number, the shocks move back along the probe, passing over the tappings (at which point the measured static pressure will drop abruptly) followed by locally supersonic flow. Before the shock passes, an additional error may be introduced into the measured pressure due to the interaction of the shock with a laminar boundary layer. The effect may be reduced by fitting a trip ring to the nose of the probe to promote a turbulent boundary layer that is more resistant to the passage of the shock, or eliminated by using a fine-nosed probe for high-subsonic freestream flows ($M \leq 0.8$, [4.1]).

Allen and *Hooper* [4.5] investigated probes of differing geometries, concluding that the dependence of the behaviour on the mean velocity distribution and the angular sensitivity (of all designs except a sphere) implied that individual calibrations were required for all but the well-documented *standard* design of Fig. 4.1b.

Note that the Venturi effect caused by the blockage due to the probe body may also influence the pressure measured using a static tube in confined flows.

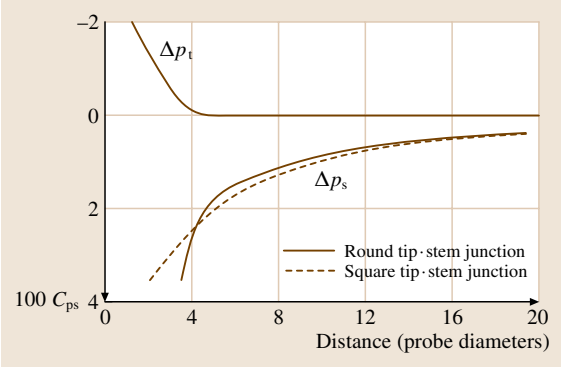

Fig. 4.8 Percentage error in the measured pressure, i. e., $100C_{ps}$, due to the effect of tip (Δp_{tip}) and stem (Δp_{stem}) on pressure measurement by static tube (or Pitot static probe) (After *Pope* and *Harper* [4.21])

4.2.2 Effect of Hole Location

The downstream location of the holes relative to the probe tip and stem will influence the measured pressure if the separation from either is too small. Flow in the immediate vicinity of the tip undergoes a local acceleration and a tapping in this region will record a pressure that is significantly lower than the true value for several probe diameters d downstream of the tip (although note that this distance will have some dependence on tip geometry). Figure 4.8 shows a typical variation of the percentage error, $100C_{ps}$, induced by the tip flow (labelled Δp_{tip}) in terms of the separation of the static hole and the tip in probe diameters. *Liepman* and *Roshko* [4.22] suggest that the holes should be $10–15d$ downstream of the nose to eliminate this error.

The effect of the stem on the pressure reading is in the opposite sense: approaching flow experiences a pressure rise due to local deceleration. This effect is more persistent (Δp_s as shown for two stem/probe geometries and tappings in the plane of the stem axis in Fig. 4.8).

Probes may be designed such that the tip and stem errors cancel, as in so-called Prandtl probes. *Pope* [4.21] suggests that for this type of probe the errors will cancel if the static holes are located $6d$ downstream of the tip and $8d$ upstream of the stem.

The tappings will normally have a depth of order $\mathcal{O}(d/2)$, greater than twice the orifice diameter, d_s, such that the deep hole tapping correction will be applicable (Sect. 4.1.2). Note that the generally shallow depth of the cavity behind the orifice implies that the measurements will be particularly sensitive to burrs, both internal and external.

4.2.3 Directional Sensitivity

By the nature of the quantity static tubes are designed to measure, they are quite directionally sensitive. Flow around ellipsoidal nose designs separates later than around hemispherical tips and thus the former are less sensitive to yaw (in the sense of smaller errors for moderate yaw $< 15°$, but note that at larger yaw angles the error increases rapidly and exceeds the hemispherical nose value). The use of several holes around the circumference of the tube decreases this sensitivity, but in any case accuracy in the region of 1% in C_{ps} can be obtained for a yaw of less than 5° in turbulent flow, or 2% for yaw less than 26° in the plane normal to the hole axes for a round-nosed tube [4.1]. If the incoming flow is laminar, probes exhibit a narrower angle of approximately

constant C_{ps}, followed by a faster increase in error for larger yaw angles [4.20].

4.2.4 Effect of Turbulence

While the effects of turbulence on measurements made with static tubes remain somewhat unclear, it can be determined that the influence will depend on the distribution of turbulent energy between the components (only the normal components, $\overline{v'^2}$ and $\overline{w'^2}$, contribute for a correctly aligned probe), eddy size in relation to the probe diameter (or more specifically to the separation of static tappings) and turbulence intensity.

Proposals for the form of the error have been given for eddies that are small (and uncorrelated at the measurement locations) [4.23, 24] and large (such that a simple quadratic yaw response is appropriate) [4.25]:

$$C_{ps} = +\frac{1}{2}\frac{(\overline{v'^2}+\overline{w'^2})}{U^2}, \quad d/D \text{ large}$$

(*Fage* [4.24])

$$= -\frac{1}{2}\frac{(\overline{v'^2}+\overline{w'^2})}{U^2}, \quad d/D \text{ small}$$

(*Bradshaw* and *Goodman* [4.25], after Toomre). (4.10)

However *Christiansen* and *Bradshaw* [4.20] indicate that $C_{ps} = 0 \pm 2\%$ for ellipsoidal-tipped probes in the range of eddy-size-to-probe-diameter ratio that would be used in common practice. They also noted that the error should be expected to increase as the square of turbulent intensity by (4.10).

4.3 Hardware and Other Considerations

The accuracy of pressure measurements depends critically on the sensitivity of the transducer employed. For high precision, fast response times and a digital output, diaphragm-type transducers are the preferred choice, although the proportionality of sensitivity to the full-scale reading means that high-range transducers give poor accuracy in flows with low velocities. In addition, the effect of temperature on zero drift must be considered, such that calibration in situ using reference pressures may be required. Liquid manometers tend to be larger and slower to respond to input pressures.

For measurements at multiple locations, multichannel devices such as the older mechanical scanning Scanivalve systems or newer multisensor units permit sequential and simultaneous measurements, respectively. Alternatively, a bank manometer may be used.

The exact configuration of the probes and accompanying hardware, including the transducer, traversing system, position encoder etc., will depend on the flow under consideration: in a large, low-speed wind tunnel, they may all be mounted inside the test section downstream of the measurement location, whereas for confined flows only the probe(s) will be inserted into the flow and connectors will lead outside to the transducer.

The connections between probes and transducers are commonly made using flexible, plastic tubing (where the exact material may be selected based on the temperature requirement) when moderate pressures are involved, or metal tubing for higher pressures. Care should be taken that the tubing is sufficiently thick to avoid kinking due to the path between probe and transducer and/or failure due to the pressure difference across the wall. The response time of the system may be optimised by minimising the volume between probe and transducer without reducing it so much that the flow required to adjust to a new pressure experiences significant resistance [4.1].

Techniques for the measurement of steady pressure using wall tappings and static tubes have been described here. For information on the determination of velocity magnitude and direction from pressure measurements using Pitot tubes, Pitot static probes, multihole probes and yawmeters the reader is referred to Sect. 5.1 and *Chue* [4.2].

4.4 Pressure-Sensitive Paint (PSP)

4.4.1 Basics of PSP

General

Wind-tunnel tests are designed to give aerodynamicists information about the performance of a model when subjected to airflow. Such testing is vital in the development of new aircraft, cars, etc. in the prediction of performance and manoeuvrability, and in the identification and resolution of aerodynamic problems. Aspects of interest include structural loading, aerodynamic efficiency, boundary layer and transition effects, and the validation of computational fluid dynamic (CFD) codes. Pressure measurements made on the surface of wind tunnel models play an important role, particularly in the development of wing design and when covering the complete model surface, forces and moments. Since first basic tests in the early 1990 other applications of pressure and temperature measurements (PSP/TSP) have been performed, such as PSP/TSP tests on the blades of turbo machines or transition measurements in cryogenic wind tunnels, which requires TSP for very low temperatures or very low concentration of oxygen for PSP measurements.

Conventionally, surface pressures are measured [4.26] using hundreds of pressure taps. These are connected to mechanical or electronic scanning systems mounted within the model or, for highest accuracy, large secondary standard pressure transducers mounted externally to the model. These orifices can influence the flow over the model and introduce measurement errors. The introduction of pressure-sensitive paint (PSP) provides a method [4.27] to measure the pressure on the surface of a model directly without the transducers and tubing. A paint, the luminescence of which is dependent on air pressure, is applied to the surface of a wind tunnel model and the pressure distribution is obtained from the images produced by proper illumination [4.28–98]. With PSP technology the potential exists for a considerable saving in the cost of model design and manufacture.

Objectives

Herein we describe the theory and practice of optical pressure measurement (PSP), summarising the work of researchers around the world in many application areas and draw on our own group's experience in the industrial wind tunnel community.

Section 4.4.2 describes the theory and practice of pressure-sensitive paint Section 4.4.3 provides an understanding of paint excitation and imaging systems, and Sect. 4.4.4 the necessary image processing techniques. Section 4.4.5 discusses some applications where optical pressure measurement is already in use.

Concepts

The method is based on the phenomenon of deactivation of photoexcited molecules of organic luminophores by oxygen molecules (quenching). The ability of oxygen to quench the luminescence of organic luminophores was discovered by *H. Kautsky* and *H. Hirsch* in 1935 [4.26]. Certain materials are luminous when excited by the correct light wavelength. This luminescence can be quenched by the addition of another material. In 1919 *Stern* and *Volmer* [4.99] published a paper describing the physics behind this phenomenon and a set of equations that model it. In 1980 *Peterson* and *Fitzgerald* [4.100] used a luminescent dye sensitive to oxygen quenching to visualise a jet of oxygen flowing over a surface.

In 1985 *Pervushin* et al. [4.101] used oxygen quenching to measure the pressure of air on the surface of wind tunnel models. This was the first time a pressure-sensitive paint was used as a tool for aerodynamic research. Subsequent advances in imaging technology, notably high-resolution charge-coupled device (CCD) cameras and digital image processing, have made this technique accessible to more users. Finally a coating that can be applied to the model surface like an ordinary paint is necessary. A comparison of accuracy is usually carried out against measurements performed with conventional pressure orifices. However, various problems have to be considered during the covering of pressure tapped models with PSPs. The orifices may be protected by covering them with small pieces of an ordinary adhesive tape before PSP application, but after removing these pieces sharp edges of PSP occur in the vicinity of pressure tap orifices (Fig. 4.9a). The orifices may also

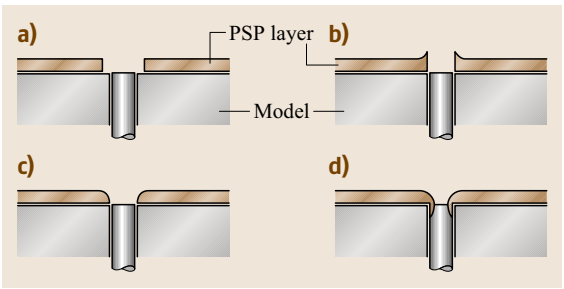

Fig. 4.9a–d Paint formation around a pressure tap orifice at different means of orifice protection

be protected by inserting wire pieces of an appropriate diameter before PSP application, but the PSP then forms hillocks around the orifices (Fig. 4.9b). The alternative way to protect the pressure tap orifices from being covered by the PSP is to blow air through the taps during PSP application, but this creates craters of PSP around the orifices (Fig. 4.9c). Moreover, blowing air can be performed only if the other sides of the pressure taps are accessible. Experience of numerous experiments shows that spraying of PSP as a thin polymer layer does not damage pressure taps without any orifice protection and does not changes their shape significantly (Fig. 4.9d) since the total thickness of PSP is usually 20–60 μm.

Deformations of the model and the model support take place under aerodynamic loads in the airflow. These deformations cause deformation and displacement of the model image acquired in the airflow. A set of markers must be established on the PSP surface to be able to correct for the displacement and deformation of model image during image processing [4.27]. Characteristic points of the model image may be used as markers, but the restricted number of these does not allow adequate correction of the model image. It is more reasonable to generate the necessary number of these markers, uniformly distributed on the model surface, as clearly identifiable points on the PSP surface; markers can be made using luminescent points on the model surface with very high luminescence intensity, but some may then be lost during image recording since the measurement system is adjusted to obtain a luminescence signal as close to the maximum signal of the image detector as possible. Thus, it is preferable to make markers as contrasted, dark points on the PSP-coated surface. They may be made by covering some points of the model surface with small pieces of an ordinary adhesive tape during active layer application and removing these after drying of the active layer. The number and position of markers required depend on the processing algorithm, while their size depends on the spatial resolution of the image detector and has to allow a precise enough measurement of their position on the model's image. Knowledge of the correct coordinates of the markers on the model surface allows transformation of the bidimensional pressure distribution on the model image to the three-dimensional pressure distribution on the real model geometry.

The deformation of the model and the model support also causes a change of the excitation light intensity distribution on the model surface. This change must be corrected in the case of the luminescence intensity acquisition to avoid additional errors during pressure reconstruction. For this purpose, a few spots of reference

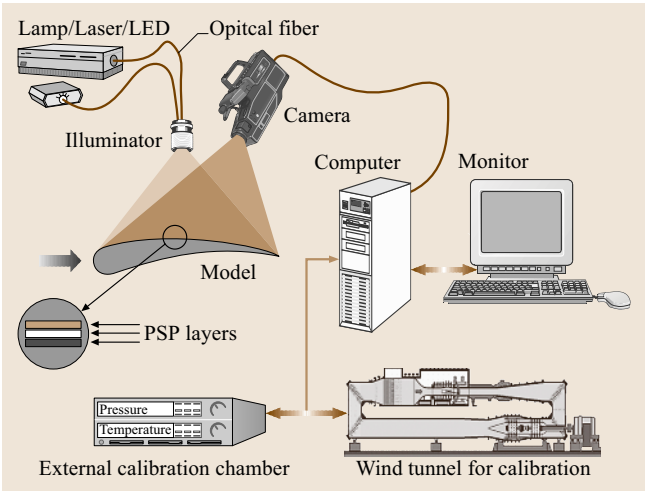

Fig. 4.10 Schematic of pressure-sensitive paint measurement system

luminescent material, insensitive to pressure and temperature, may be placed on the model surface in regions of less interest. The number of spots depends on the processing algorithm, while their size depends on the spatial resolution of the image detector and has to allow a precise enough measurement of their luminescence intensity. If a change of the excitation light intensity does not exceed a few percent, a restricted number of luminescent references allows precise enough determination of the correction function for the excitation light intensity.

The painted model may be stored for an extended period of time, being protected from external light, dust and contact with any undesirable materials (oil, solvents, other polymeric materials, etc.). Illumination of the paint initiates photochemical reactions inside the active layer that causes photodegradation of its components and thus the loss of its pressure-sensitive properties under an extended period of illumination. The best way to keep the model is to place it in an opaque box, and store it in complete darkness at 20–80% relative humidity.

The schematic of the test setup in Fig. 4.10 shows all the essential optical and electrical components of a PSP system. The system consists of various illumination devices, twin CCD cameras or filter wheels for pressure and reference images (because of the use of binary paint, with pressure-sensitive molecules and reference molecules without pressure and temperature dependency), a local image and data-acquisition system and an external calibration chamber, if possible, to pressurise the wind tunnel, the test section can also be used for full-size model calibration. In order to be

applicable to the widest possible range of wind tunnel tests modular and highly sophisticated acquisition and processing subsystems are required. User-friendly software packages have already been developed by various users.

4.4.2 Paints

General Description

Figure 4.13 shows a basic schematic of the processes of luminescence and oxygen quenching. A pressure-sensitive paint consists of a dye held in an oxygen-permeable binder. The dye absorbs light, and the energy is used to shift an electron from one part of the molecule to another. The former part of the molecule gains a positive charge with a negative charge on the latter and these are stabilised and held apart. For ruthenium-based paints the excitation wavelength is in the blue ($\lambda = 450\,\text{nm}$) and the emission wavelength in the red ($\lambda = 620\,\text{nm}$), For pyrene-based paints the excitation wavelength is in the ultraviolet (UV, $\lambda = 340\,\text{nm}$) and the emission wavelength is in the blue ($\lambda = 450\,\text{nm}$). The molecule becomes a tiny battery that will discharge a photon by the process of luminescence after a characteristic lifetime. The paint is seen to glow. The battery can also be discharged without luminescence by a collision with oxygen. The higher the oxygen partial pressure the less the paint glows. The intensity of the luminescence gives a measure of the partial pressure of oxygen and hence the pressure of the air.

If the paint is illuminated with a pulse of light the luminescence will decay exponentially with a characteristic lifetime. This lifetime is also quenched by oxygen. The higher the oxygen pressure the shorter the lifetime as the dye molecules loses energy by collision with oxygen instead of luminescence.

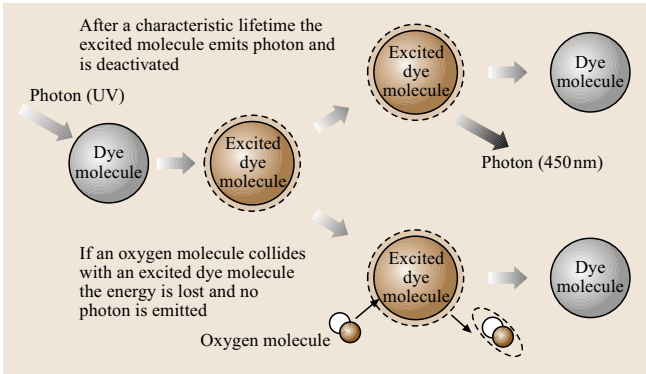

Fig. 4.11 Schematic of oxygen quenching

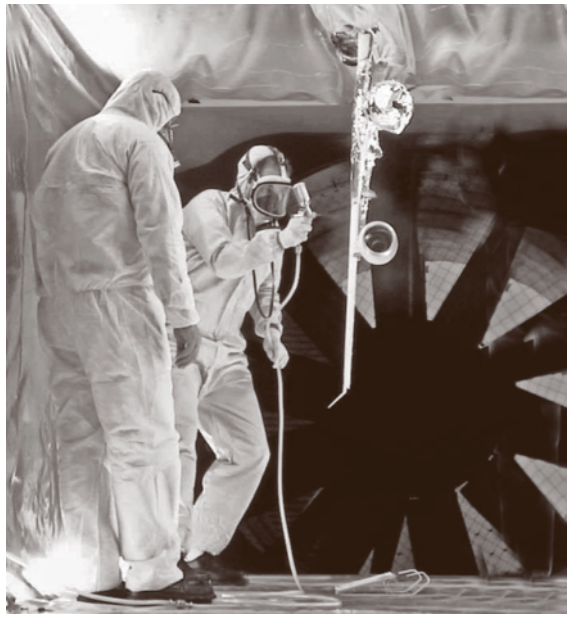

Fig. 4.12 PSP paint spraying in the covered test section itself

Pressure-Sensitive Paint Realisations

To utilise the phenomenon of dye-molecule quenching by oxygen to create pressure-sensitive sensors it is necessary to solve three closely related problems.

1. It is necessary to find such dye molecules and to place them in such a binder that quenching collisions between oxygen and dye molecules become probable during the lifetime of an excited dye molecule. If these collisions are improbable, no effect of oxygen pressure on luminescence will be observed. On the contrary, if large numbers of these collisions take place, no luminescence can be seen. This means that both very low- and very high-sensitivity paints do not allow highly accurate pressure measurements and that there is an optimal pressure sensitivity of the PSP that allows a minimum pressure measurement error.
2. Dye molecules should be attached to the model surface and the PSP layer should withstand both normal and tangential loads of the airflow. To increase the luminescent signal, and thus the accuracy of the measurements, the number of dye molecules must be as large as possible but these molecules must not affect each other. There are two different methods to attach dye molecules to the model surface: to spread them into a polymer binder or to adsorb them on a microporous surface.

Table 4.1 Historical review of paint development

Luminophore	Binder	Mechanical properties	Ref.	Year
Trypaflavin	Silicagel	Powder	[4.101–103]	1964
Pyrene, coronene, p-terphenyl	Mineral oil, apiezon, decaline, glycerol, silicagel, alumina, molecular sieves	Viscous liquid, powder	[4.104]	1971
Anthracene	solution	Liquid	[4.105]	1974
Platinum group metal complexes; porphyrin and phthalocyanine complexes of VO^{+-}, Cu^{++}, Zn^{++}, Pt^{++}, Pd^{--}; dimeric Rh, Pt, Ir complexes.	Plexiglas, polystyrene, polycarbonate, resins, polyvinylchloride, latex, teflon, polypropylene, polyvinylidene, fluoride, silicon rubbers	Films	[4.106]	1986
$[Ru(Ph_2phen)_3](ClO_4)_2$	GE RTV SILASTIC 118	Film	[4.106]	1986
PtOEP, PdOEP	Polysterene	Film	[4.107]	1995
$[Ru(Ph_2phen)_3](ClO_4)_2$	Polystyrene	Film	[4.108]	1995
$Ru(bipy)_3^{++}$	Zeolite+silicone	Paint, film	[4.109]	1995
$[Ru(Ph_2phen)_3](ClO_4)_2$ $Ru(bipy)_3^{++}$	Silicagel+silicone	Paint, film	[4.109]	1995

3. To provide optimal pressure sensitivity the dye and the binder of the PSP should be chosen to provide optimum quenching conditions. The polymer binder or the microporous surface on the one hand restrict the probability of the oxygen–dye collisions that determine the pressure sensitivity of a luminescent pressure sensor and on the other hand affect dye molecules by changing their luminescence characteristics. The oxygen permeability of the binder also affects the time response of the PSP to a pressure change, so highly permeable polymers and absorbers are preferable to decrease the PSP response time. Also, the probability of oxygen luminophore collisions increases the oxygen permeability of the binder, so the luminophore lifetime should be of an appropriate range to create a PSP using a highly permeable binder. Chemical immobilisation of dye molecules in the polymer binder or on the microporous surface to provide the required dye concentration while preventing interaction of the dye molecules with each other is also a rather complex problem. A further problem is the technology for the application of a selected luminophore–binder system to the model surface. To use a PSP in aerodynamic research it should be relatively thin, smooth and should adhere sufficiently well to the model surface. To perform accurate pressure measurements with pressure-sensitive sensors it is also very important to provide the same PSP characteristics at all points on the model surface.

Oxygen Sensors. There exist a number of luminescent oxygen sensors for medicine, biology, environmental monitoring and industrial process control. Some of the most important are presented in Table 4.1.

As we will see later these systems are widely used in pressure measurements. The first oxygen sensors were liquids or powders and could not be used in aerodynamic research. Analysis of the latest publications shows that the most promising luminophores are platinum or palladium porphyrins (PtOEP, PdOEP) and ruthenium complexes such as tris-4,7-diphenyl-1,10 phenathroline ruthenium(II) ($[Ru(Ph_2phen)_3,]^{++}$) or tris-2,2'-bipyridyl ruthenium(II) ($Ru(bipy)_3$) and the most preferable binder is silicone rubber.

Dyes. Pressure-sensitive paints appear to be divided into three families, using ruthenium polypyridyls, platinum/palladium porphyrins or pyrene derivatives for dyes. Figure 4.13 shows the structure of these dyes. The ruthenium compounds are excited in the blue, glow red and are very photostable. However, they are difficult to incorporate into polymer systems and have a low sensitivity to oxygen. The porphyrin compounds may be excited in the UV or the green and produce a red luminescence. They have long luminescent lifetimes and are very sensitive to oxygen but often have low signal strength at atmospheric pressure. The pyrene derivatives are UV excited, have luminescence in the blue and have the best thermal stability, but suffer from photodegradation.

Binders. The key to a successful pressure-sensitive paint lies in the choice of an appropriate binder. The binder should be

- stable, with a long shelf life
- compatible with and adhere to the materials in wind tunnel models
- safe to apply
- quick to cure without the application of high temperatures
- aerodynamically smooth
- highly permeable to oxygen
- safely and easily removable with no damage to the model

Researchers tend to use dimethylsiloxane polymers, as these have high oxygen permeability. These polymers are used widely by industry and come in a variety of forms. Room-temperature-curing polymers use a catalyst, often atmospheric moisture, to polymerise [4.110]. These rubbers contain powerful adhesives that bind to many substrates. They may be self-levelling but cannot be polished. Other thermally activated polymers cure to form a hard surface that can be polished flat. However, the application of heat is detrimental to wind tunnel models covered by such binders.

Solvents. A solvent is used to dissolve the dye and the binder. It also thins the paint so that it can be sprayed and evaporates to leave a homogenous layer of paint. Most pressure-sensitive paints use chlorinated organic solvents such as dichloromethane and trichloroethane. Dichloromethare is the active constituent of paint stripper and allows the dye to dissolve by expanding the polymer. The use of alcohol has also been reported [4.109].

Manufacture and Spraying

The order in which the components are mixed is very important during PSP manufacture. The relative concentrations of dye, polymer and solvent can also change the paint characteristics. Low dye concentration will reduce the signal from the paint while high dye concentration causes the paint to self-quench, reducing the paint luminescence.

Pyrene- as well as ruthenium-based paints were developed in combination with special binders to minimise their polymerisation time, permeability and lack of photodegradation.

For normal paint, which means for transonic use, we mainly use pyrene-based paint as well in a polymer binder as in anodised aluminium (AA). The function of the polymer binder has been explained above, and Fig. 4.12 of the structure of AA from *Sakaue* [4.111] should give an impression. It is possible to create very small holes like an open sponge in a thin aluminium surface. For anodisation processing with H_2SO_4 is first necessary, followed by treatment with H_3PO_4.

It is possible to put pressure-sensitive dyes into these holes. Oxygen has to penetrate via diffusion from the top into the holes. Compared with other so-called *open systems* the response time is very short (50 µs to 1 ms) and therefore this type of paint is a good candidate for unsteady PSP.

An electrochemical process is applied to obtain an anodised aluminum layer, which is formed on an aluminum anode in an electrolytic solution. A self-ordered structure is obtained using this anodisation at a constant direct current in the electrolyte at a constant voltage (i. e. electrolyte temperature).

There are a huge number of micropores on the surface. This anodised aluminum is formed using dilute sulfuric acid as electrolyte. The anodising voltage was 20 V, and the current density was 12.5 mA/cm^2. The anodising time was about 30 minutes. The diameter of the micropores is proportional to the anodising voltage. The depth of the anodised aluminum is proportional to the anodising time, with a constant voltage and a constant current density.

In order to create uniformly distributed micropores as shown in Fig. 4.12, it is necessary to conduct careful pre- and post treatments. The porous anodised aluminum layer is optically transparent if the diameter of micropore is much less than the wavelength of light. The anodised aluminum layer is also formed on aluminum alloys that contain Mg, Fe, Cr or Si, though the structure of the micropores is somewhat disordered [4.112].

Nonperiodic unsteady pressure is difficult to measure using the PSP technique, even though several attempts have been made to measure an unsteady pressure field [4.113, 114]. The most serious problem with unsteady measurement is that the signal from the PSP is inevitably weak due to the short exposure time. As for periodically fluctuating measurements, accurate pressure data can be obtained using phase-locking methods. In such a case, several snapshots at a given phase angle are superposed in a single image until sufficient light is accumulated. However, today the superposition technique is no longer applied to nonperiodic phenomena.

Temperature and *humidity* effects on the PSP signal are other issues. The temperature effect causes substantial errors in all PSP measurements. On the other hand, sensitivity to humidity is not negligible in the

AA-PSP, because the anodised aluminum layer has a hydrophilic nature. The moisture content in the layer alters the oxygen concentration in the AA-PSP. We carefully examine the acquisition and processing of PSP images to eliminate these errors.

Another *open system* has been developed by German Aerospace Center (DLR) [4.115], at first for cryogenic use, which is sprayable like the well-known steady paints. One new type of pressure-sensitive dye is palladium tetra-(pentafluorophenyl)porphine (PdTFPP) embedded in a porous binder of poly(trimethylsilyl-propyne) [poly(TMSP)] – for very high oxygen permeability.

Schanze [4.116] published a paint formulation based on the dye tris(4,7-diphenyl-phenanthroline) ruthenium (d) dichloride (RuDPP) in poly(dimethyl siloxane). The paint is made by dissolving 3 mg of RuDPP and 1 g of DMS-D33 in 4 ml dichlorometharic solvent. The paint is applied with an airbrush and allowed to dry for 24–48 h in low-humidity conditions.

A US patent [4.108] describes many different ways of producing pressure-sensitive paints, both with and without silica gel encapsulated in rubber. For example, the dyes pyrene and perylene were dissolved in Dow 732 silicon rubber. The paint is made by first dissolving 1 g Dow 732 silicon rubber in 7 g isooctane solvent. The resulting solution is shaken and placed in an ultrasonic cleaner for 15 min. 1.5 mg of pyrene and 1.8 mg perylene are added and allowed to dissolve. The paint is applied with an airbrush and allowed to cure at ambient temperature and humidity.

Kavandi et al. [4.117] published a paint formulation based on the dye platinum octaethylporphyrin (PtOEP) from Porphyrin Products, USA, in a poly(dimethyl siloxane) solution GP-197. The paint is made by mixing 0.1 g of PtOEP in one litre of GP-197 solution. The dye quickly dissolves to give a dark-red solution. The paint is applied by airbrush and cured at 100 °C for 2 h. *McLachlan* et al. [4.118] mixed a fine powdered rutile-grade TiO_2 into this paint to improve the signal strength 2.5 times by increased scattering.

Spraying Procedure

PSP is usually applied to a wind tunnel model by an adhesive layer or spraying using professional airbrushes like those used by car painters. The selection of the nozzle diameter as a function of the actual air pressure is very important.

Pressurised air for the system must be clean and free of compressor oil. The airbrush can be cleaned by various solvents, such as acetone. The uniformity is judged by eye and spraying will be stopped when a good colour is seen. In most cases a neutral blue pigment [4.99] is added to the final layer and thickness can be controlled easily on a white background layer by the intensity of the blue colour.

Various instruments for measuring the coating thickness can be used after curing. A typical total thickness for steady measurements is 40–60 μm, although for fast paints (response time < 1 ms) the typical thickness is about 5 μm. It is common practice to fill all the screw holes and other wrinkles before a model enters a wind tunnel. Some of these surface fillers fluoresce significantly under PSP lighting, which changes the paint calibration above the filler and limits the exposure time of the carriers. The fillers themselves may also emit various wavelengths or may shrink during PSP spraying because of the various solvents in the paints. It is becoming increasingly popular to coat the model directly in the test section [4.119] (Fig. 4.14) to minimise the installation time.

A very stable filler for most existing paints was found from the Loctite Company (Fig. 4.15).

When spraying in closed rooms ventilation with absolutely dust-free fresh air is necessary. Also personal protection with a mask and an overall must be provided and safety precautions taken.

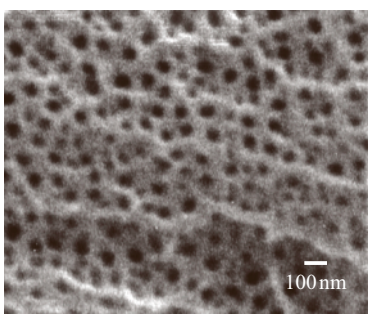

Fig. 4.13 Surface of modified aluminum (anodised aluminum)

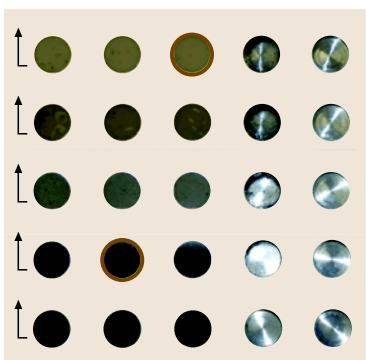

Fig. 4.14 Various fillers for stabilisation tests using PSP subsequently

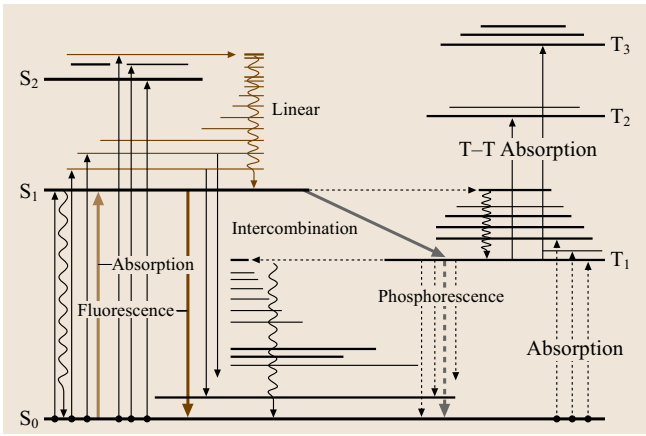

Fig. 4.15 Triplet and singlet levels and intersystem crossing

It should be pointed out that all pressure-sensitive molecules are believed to constitute a health hazard. The toxicity of the other ingredients like the solvents is not well known. In all cases, it is always recommended to avoid skin contact and inhalation during spraying.

Theory

Photophysics for the Intensity-Based System. The theory of pressure-sensitive paint luminescence is found in the photophysics of dye molecules. The theory uses the concept of quantisation of allowed molecular excitation states and electron spin. Figure 4.16 shows an idealised energy-state (Jablonski) diagram of a molecule. The vertical axis represents the molecular energy. The boxed arrows show the electron spin. For states with electron spins in opposite directions the term singlet is used. For states with electron spins in the same direction the term triplet is used.

Parker [4.120] describes the energy transfer mechanisms for molecules and notes that nearly all molecules have an even number of electrons [4.99, 120].

The electrons populate a ground, or lowest-energy, state (S_0) in pairs, with the spin of the electrons opposed. However, if one of the electrons is promoted to an upper energy state (S_1, T_1) the spin of the electrons can be in the same or opposite directions.

The solid arrows in Fig. 4.16 show radiative absorption and emission between states. The bold horizontal lines correspond to the excited states of the molecule. The fine lines correspond to the vibrational energy states of the molecule between which transitions occur by absorption and emission of long-wavelength radiation indicated by the wavy lines. This process is known as internal conversion. Radiationless intersystem crossing (a) occurs from the lowest-energy state of a singlet level (S_1) to one of the upper vibrational levels of the lowest triplet level (T_1). From here the molecule quickly looses its excess vibrational energy. The rate of intersystem crossing can successfully compete with the rate of fluorescence in some molecules.

At first sight it appears that radiationless intersystem crossing (b) $T_1 \rightarrow S_0$ should be just as fast as possible. In fact it occurs at least 10^8 times slower and is the reason that phosphorescence can be observed.

$\longrightarrow$ Radiative decay
k_P = phosphorescence and
k_F = fluorescence

$\dashrightarrow$ Radiationless decay
k_{IC} = internal conversion $S_1 \rightarrow S_0$
k_{ISC} = intersystem crossing $S_1 \rightarrow S_0$
k'_{ISC} = intersystem crossing $S_1 \rightarrow S_0$
$k_{thermal}[T]$ = thermal deactivation
$k_Q[Q]$ = quenching

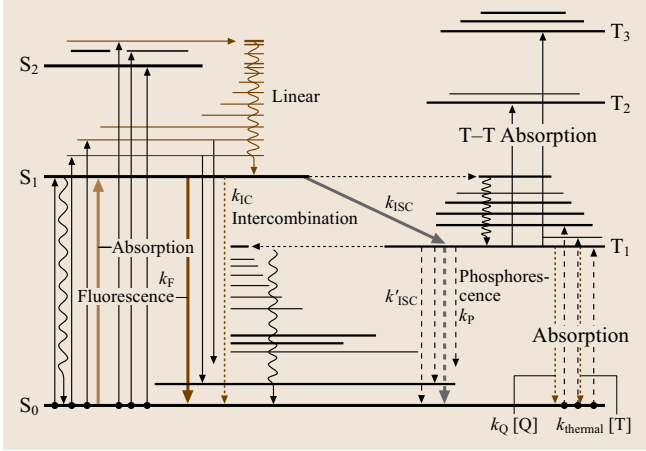

Fig. 4.16 Schematic of possible energy paths

Rate Factors and Quenching Processes. Figure 4.15 shows the relevant intramolecular decay step mechanisms for pressure-sensitive paint, each characterised by its own rate constant. Each excited state is characterised [4.121] by its lifetime, given by

$$\tau = \frac{1}{\sum k_i} , \qquad (4.11)$$

where k_i is the rate constant for a generic molecular process that causes the disappearance of the excited state.

The quantum yield for each luminescence process is the ratio between the number of photons produced to the number of photons absorbed. For example the quantum

yield Φ_P for phosphorescence from the lowest excited triplet state is:

$$\Phi_P = \eta_{ISC}\eta_P \,, \tag{4.12}$$

where η_{ISC} is the efficiency with which the triplet state is populated by light absorption and η_P is the efficiency of phosphorescence from the triplet state. These efficiencies are computed by determining the ratio of the desired energy path to the sum of all energy paths. By inspecting Fig. 4.17

$$\eta_{ISC} = \frac{k_{ISC}}{k_{ISC} + k_F + k_{IC}} \tag{4.13}$$

and ignoring thermal effects $k_{thermal}(T)$ and quenching $k_Q[Q]$ to simplify this step

$$\eta_P = \frac{k_P}{k'_{ISC} + k_P} = k_P \tau_{T1} \,, \tag{4.14}$$

where τ_{T1} is the lifetime of the excited triplet state.

When the lifetime of the excited state is sufficiently long the excited molecule may have the chance to encounter a molecule with which to interact to allow deactivation without radiation. This is called bimolecular quenching. If $k_Q[Q]$ is the quenching rate and [Q] is the concentration of the quencher then (4.14) can be modified to

$$\eta'_P = \frac{k_P}{k'_{ISC} + k_P + k_Q[Q]} \,. \tag{4.15}$$

Stern–Volmer Relations. *Stern* and *Volmer* [4.99] noted that, if the ratio of the die luminescent intensity with a quencher I and without a quencher I_0 was plotted against the quencher concentration, then a straight line was obtained. By definition the quantum efficiencies are directly proportional to the luminescent intensity. Taking the ratio of (4.12) with and without the quencher and substituting in (4.14) and (4.15) gives the equation of a straight line

$$\frac{I_0}{I} = \frac{\eta_{ISC}\eta_P}{\eta_{ISC}\eta'_P} = \frac{\frac{k_P}{k'_{ISC}+k_P}}{\frac{k_P}{k'_{ISC}+k_P+k_Q[Q]}} = 1 + \frac{k_Q[Q]}{k'_{ISC}+k_P} \,. \tag{4.16}$$

The lifetime of the phosphorescent state is computed using (4.11) by inspection of Fig. 4.17, again ignoring thermal effects

$$\tau = \frac{1}{k'_{ISC} + k_P + k_Q[Q]} \,. \tag{4.17}$$

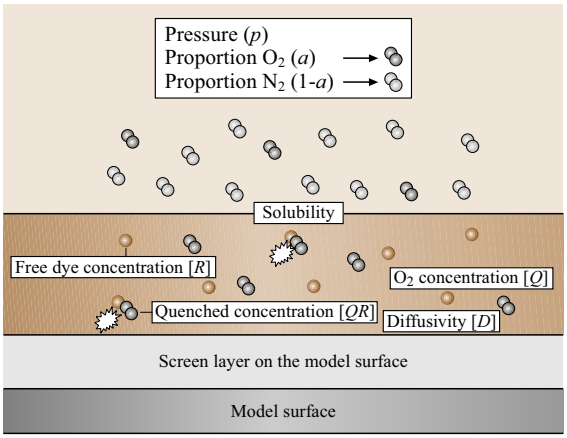

Fig. 4.17 Schematic of paint photochemistry

Taking the ratio of the lifetimes with a quencher τ and without quenching τ_0 reveals another Stern–Volmer equation:

$$\frac{\tau_0}{\tau} = \frac{\frac{1}{k'_{ISC}+k_P}}{\frac{1}{k'_{ISC}+k_P+k_Q[Q]}} = 1 + \frac{k_Q[Q]}{k'_{ISC}+k_P} = 1 + \tau_0 k_Q[Q] \,. \tag{4.18}$$

Comparing (4.16) with (4.18) and noting that (4.16) assumes that η_{ISC} is unchanged between the two measurements of I_0 and I it is seen that the intensity and lifetime ratios follow the same equation:

$$\frac{I_0}{I} = \frac{\tau}{\tau_0} = 1 + \tau_0 k_Q[Q] \,. \tag{4.19}$$

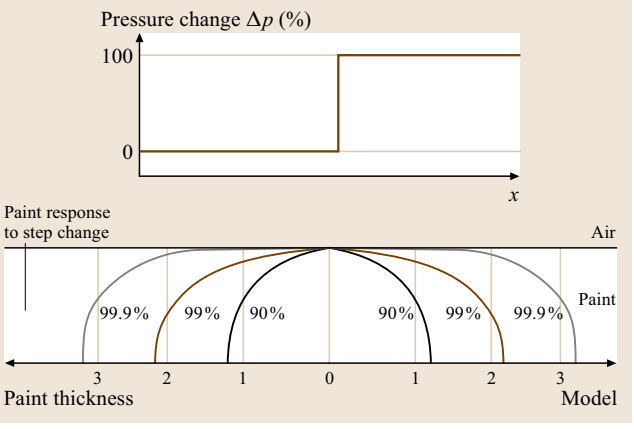

Fig. 4.18 Response of pressure-sensitive paint to spatial step change in pressure

Photochemistry. *Wolfbeis* [4.122] predicts the basic behaviour of immobilised indicators (dye molecules held in a matrix) that are quenched by a dissolved gas. A schematic of this process is shown in Fig. 4.18. An equilibrium is established between the concentrations of the quencher molecules [Q], unquenched indicator molecules [*R*] and the associated quenched complex [QR]. Assuming a 1:1 stoichiometry, the equilibrium is described by

$$K_{\mathrm{E}} = [\mathrm{QR}]/[\mathrm{Q}][\mathrm{R}]\,, \tag{4.20}$$

where K_{E} is the equilibrium constant.

The total concentration [C] of the immobilised indicator is the sum of the free and complexed molecules

$$[\mathrm{C}] = [\mathrm{R}] + [\mathrm{QR}]\,. \tag{4.21}$$

If the total amount of indicator remains constant it follows that rearranging (4.20) and substituting into (4.21) gives

$$[\mathrm{C}] = [\mathrm{R}](1 + K_{\mathrm{E}}[\mathrm{Q}])\,. \tag{4.22}$$

If the dissolved gas can quench the luminescence from the indicator then the luminescence I will be proportional to the concentration of the unquenched indicator. If there is no dissolved gas then [R] = [C] and the luminescence I_0 will be proportional to the concentration of the indicator. Substituting I and I_0 into (4.22) yields an equation equivalent to the Stern–Volmer equation [4.99]:

$$\frac{I_0}{I} = 1 + K_{\mathrm{E}}[\mathrm{Q}])\,. \tag{4.23}$$

The coefficient K_{E} can be expanded to be the product of the lifetime τ_0 of the indicator in the absence of quenching gas and the bimolecular quenching constant k_{Q} by comparison to (4.19).

Wolfbeis noted that k_{Q} is related to the collisional frequency of quenching by a modified Smoluchowski equation

$$k_{\mathrm{Q}} = \frac{4\pi\gamma NDr}{1000}\,, \tag{4.24}$$

where γ is a factor that accounts for the quenching efficiency of a collision, N is Avagadro's number, D is the diffusion coefficient of the quencher (the indicator is immobilised) and r is the collision radius. The term $N/1000$ converts molarity into molecules per cubic centimetre. For pressure-sensitive paint the concentration of the quenching gas in the polymer [Q] is equal to the product of the solubility S of the gas and the partial pressure of gas outside the polymer (Henry's law). It should be noted that Henry's law only holds for sparingly soluble gases at low partial pressures. This assumption is used to simplify the analysis. Real systems tend to have a second-order relationship between solubility and partial pressure [4.123].

The total pressure p of the air outside the polymer is equal to the sum of the partial pressures of its constituents. Equation (4.23) can be rewritten:

$$\frac{I_0}{I} = 1 + Kp\,, \quad K = \tau_0 \frac{4\pi\gamma NDr}{1000} Sa\,, \tag{4.25}$$

where a is the volume fraction of oxygen in the air, and K is the pressure sensitivity of the system and has units of reciprocal pressure.

Why Oxygen Quenching? *Ranby* and *Rabek* [4.124] give an introduction to the structure of molecular oxygen. Oxygen exists in the atmosphere predominantly as a diatomic structure and is paramagnetic. In this way oxygen differs from other permanent gases. This property is interpreted as being due to its two outer electrons having parallel spins. This uncoupled electron pair classifies oxygen as a triplet in its lowest-energy state.

The next two higher-energy states are singlets and are located 22.5 and 37.5 kcal/mol above the triplet state. This makes the excitation of oxygen relatively easy. Oxygen can successfully quench red dye luminescence by the transfer of excess energy from the dye to the oxygen molecules. *Turro* [4.125] notes that ground-state molecular oxygen is a general and efficient quencher of both singlet and triplet states of organic molecules. The process of quenching can occur in many ways; it is not even dependent on the luminophore, giving 22.5 kcal/mol as the triplet O_2 will catalyse intersystem crossing from the singlet to the triplet state.

Characteristics

Thermal Sensitivity. The quantum efficiency and lifetime of radiation from a dye are both temperature dependent [4.126]. The efficiency of $T_1 \rightarrow S_0$ phosphorescence is critically dependent on temperature and is observed to decrease by several orders of magnitude between cryogenic and room temperatures.

This is due to the long lifetime of the triplet state that allows the possibility of thermally activated, radiationless transition with a rate k_{thermal} (Fig. 4.17). The rate constant for thermal deactivation can be modelled by the Arrhenius formula

$$k_{\mathrm{thermal}} = k_0 + A\exp(-\Delta E/k_{\mathrm{B}}T) \tag{4.26}$$

where k_0 and A are constants, ΔE is the energy for the deactivation mechanism, k_B is Boltzmann's constant and T is the temperature (Kelvin).

The actual thermal sensitivity of a dye can be very complex [4.125] with (4.11) containing the sum of several competing processes. However, both I_0 and τ_0 can be empirically modelled using

$$\log\left(\frac{1}{I_0}-\frac{1}{I_0'}\right)\propto-\frac{1}{T}\quad\text{and}$$
$$\log\left(\frac{1}{\tau_0}-\frac{1}{\tau_0'}\right)\propto-\frac{1}{T}\,, \tag{4.27}$$

where I_0 and τ_0 are the intensity and lifetime at temperature T (Kelvin) and I_0' and τ_0' are the intensity and lifetime extrapolated to 0 K, all with no quenching.

The pressure sensitivity of the system K is dependent on τ_0 and also on the product of the diffusion and solubility constants, which is defined [4.127] as the permeability of the matrix P

$$P = DS\,. \tag{4.28}$$

The permeability temperature dependence can be represented by

$$P = P_0\exp(-E_M/RT)\,, \tag{4.29}$$

where E_M is the activation energy of permeation, P_0 is the exponential premultiplier, R is the gas constant and T is the temperature in Kelvin.

This analysis suggests that the production of a temperature-insensitive paint is unlikely. The lifetime falls with increasing temperature while the permeability increases. This characteristic can be used to produce a paint with K that is insensitive to temperature over a limited range, but at the expense of the thermal sensitivity of I_0 and τ_0. Choosing a dye with a low τ_0 sensitivity to temperature will increase the thermal effect on K.

Pervushin et al. [4.101] produced a paint with a luminescent intensity that remains constant over a limited temperature interval, although the thermal sensitivity of K is not quantified.

Schanze et al. [4.116] concluded that for ruthenium dyes the temperature dependence is dominated by the nonradiative decay rate of the dye molecule. However, the temperature dependence of the oxygen diffusion rate also plays a strong role. They concluded that to minimise the temperature sensitivity of a paint it is necessary to design a binder to have a low activation energy for the oxygen diffusion rate.

Spatial Resolution. The diffusion of oxygen into a layer of pressure-sensitive paint is the direct analogy of heat flowing into a solid. There are many publications [4.128] which explain the models in more detail. The flow of heat and the diffusion of oxygen are both modelled by the diffusion equation

$$\frac{\partial^2[\mathrm{Q}]}{\partial x^2}+\frac{\partial^2[\mathrm{Q}]}{\partial y^2}+\frac{\partial^2[\mathrm{Q}]}{\partial z^2}=\frac{1}{D}\frac{\partial[\mathrm{Q}]}{\partial t}\,. \tag{4.30}$$

Figure 4.19 shows the distribution of oxygen in the paint layer due to a step change in pressure across the surface of the paint. It can be modeled using the diffusion equation expanded into three dimensions with $\partial[\mathrm{Q}]/\partial t = 0$:

$$\frac{\partial^2[\mathrm{Q}]}{\partial x^2}+\frac{\partial^2[\mathrm{Q}]}{\partial y^2}+\frac{\partial^2[\mathrm{Q}]}{\partial z^2}=0\,. \tag{4.31}$$

Equation (4.31) indicates that the spatial variation of oxygen is only dependent on geometry, and in the case of PSP, on the thickness of the paint. *Bukov* et al. [4.129] have determined that the paint will have reached 99% of the pressure step change across the surface of the paint in five times the paint thickness.

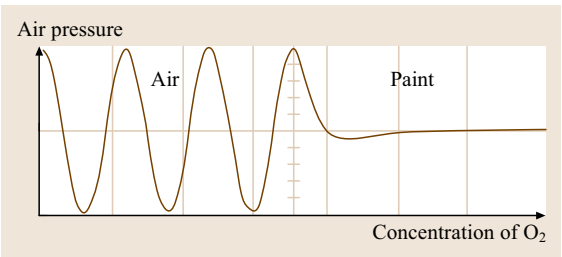

Fig. 4.19 Passage of pressure wave through an air–paint interface

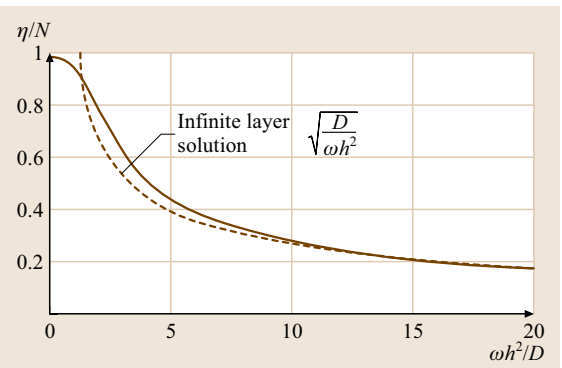

Fig. 4.20 Transfer function for pressure-sensitive paints

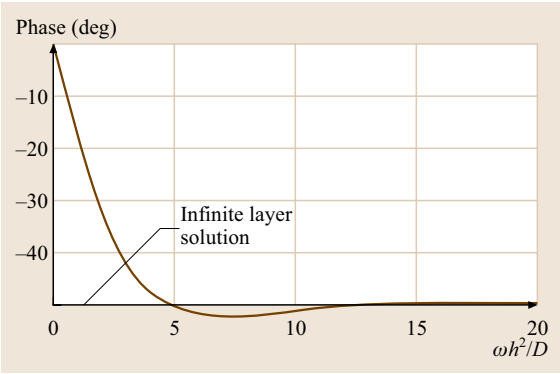

Fig. 4.21 Phase-dependent transfer function for pressure-sensitive paints

Response Time. Figure 4.20 shows a pressure wave of frequency ω impinging on the surface of a layer of pressure-sensitive paint. The passage of the pressure wave into the paint can be modelled by the diffusion equation

$$\frac{\partial^2[\mathrm{Q}]}{\partial x^2} = \frac{1}{D}\frac{\partial[\mathrm{Q}]}{\partial t}\,, \tag{4.32}$$

where [Q] is the concentration of quencher molecules in the paint and D is the diffusion coefficient. The solution to the diffusion equation is not trivial, but in this case is identical to the periodic flow of heat into a conducting solid [4.130]

$$[\mathrm{Q}](x,t) = \cos\left(\omega t - \frac{x}{\delta}\right)\exp\left(-\frac{x}{\delta}\right)\,,$$

$$\text{with}\quad \delta^2 = \frac{2D}{\omega}\,, \tag{4.33}$$

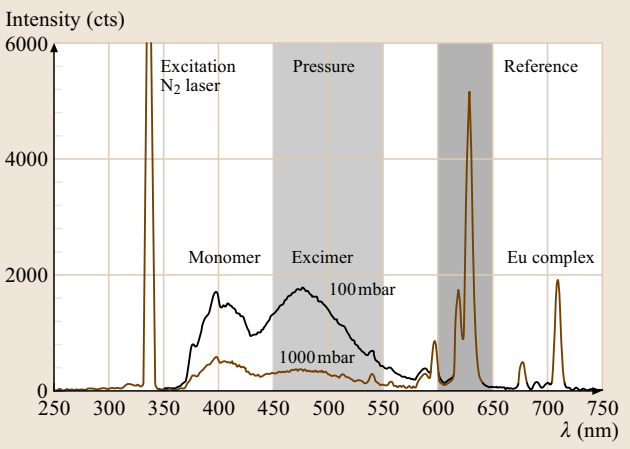

Fig. 4.22 Typical pyrene-based pressure-sensitive paint spectrum

where δ is often called the skin depth of the oscillation.

The diffusion into a finite thickness h of PSP can be modelled by applying the boundary condition $\partial[\mathrm{Q}]/\partial x = 0$ at $x = h$. As the frequency of modulation is increased, the skin depth reduces and a smaller active layer of paint is able to respond.

Equation (4.33) can be integrated over x to find the number of modulated quencher molecules n in the layer of paint. The amplitude and phase of n is plotted against the frequency factor in Fig. 4.22. In this figure, n has been normalised against the total number N of quenching molecules in the paint thickness. As ω increases the solution tends to the infinite-layer case.

This analysis concludes that the paint does not have to be thin to detect pressure fluctuations. As the frequency increases the effective sensing layer reduces in thickness. The imaging system will detect a reducing modulation on top of an increasing offset. Reducing the paint thickness does not increase the signal strength; it reduces the often observed offset. Counterintuitively, the fluctuating pressure data from thick paint would be easier to analyse than from a thin paint layer as the transfer function will be less sensitive to frequency and paint thickness.

Carroll et al. [4.131] and *Engler* [4.132] investigated experimentally the response of two pressure-sensitive paints to sinusoidal and sawtooth pressures waves. Their results agree well with this analysis.

Borovoy et al. [4.133] note that the time for a paint to achieve 99% of its response to a step change in pressure is:

$$t_{\mathrm{step}} = 12h^2/\pi^2 D\,. \tag{4.34}$$

Carroll et al. [4.104] computed the diffusion of oxygen after a step change as an infinite series of exponential functions. They found that this could be simplified to a series of two exponential functions. Several paints with varying thickness were tested to verify the dependence on thickness and diffusion rate.

Engler [4.132] conducted tests looking at the response of two paints to modulated pressures and found that OPTROD LTD. type 18E was limited to 1 Hz and OPTROD LTD. type 21-Fl could be used to measure up to 20 Hz.

Inspection of (4.25) reveals that the ideal high-bandwidth paint would utilise a binder with a high diffusion rate but a low solubility. This would keep the permeability of the polymer and the Stern–Volmer coefficient unchanged.

Spectra. The spectrum of a pressure-sensitive paint is largely due to the type of dye used. Figure 4.23 shows the spectra from a typical UV-excited phosphorescent pyrene-based dye. The emission peak is at a longer wavelength (440 nm) than the absorption peak (450 nm). The shift between the peaks is a function of the difference between the singlet and triplet energy levels. For fluorescent dyes the absorption and emission spectra can significantly overlap, which is not the case for pyrene-based dyes. The excimer peak in the range 500±50 nm is very pressure sensitive whereas the peak at 400 ± 10 nm is highly temperature sensitive. In general it is desirable for the spectral separation to be large so that broadband light filters can be used to separate the excitation light source output from the paint's luminescence.

As can be seen in Fig. 4.23, two different dyes were used: a pressure-sensitive one and a reference dye which is not pressure or temperature sensitive. The illumination for this dye is the same as for the pyrene dyes, but the emission is in the far red wavelength about 630 ± 10 nm with a high peak. Therefore it is easy to separate it from the pressure peak in the blue.

These dyes are only sensitive to the illumination intensity and are therefore an ideal reference component for illumination correction, because there is no chance of creating a stable and homogeneous illumination on the model's surface.

Also in these spectra the influence of two different pressures, red (100 mbar) and green (1000 mbar), is clearly visible and illustrates that a much higher intensity is given at 100 mbar than at 1000 mbar.

Intrusion. Pressure-sensitive paint is an intrusive technique. The finite thickness of the paint alters the profile of the aerofoil and the surface of the paint never has the same surface finish as the underlying material. These effects lead to differences in the pressure distribution on the model surface and will alter the aerodynamic drag.

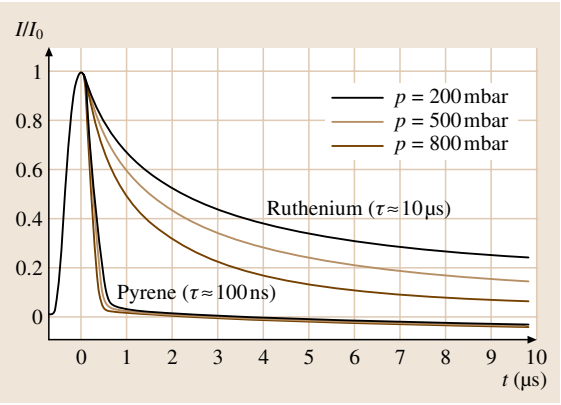

Fig. 4.23 Principle of lifetime measurement for two different dyes

These problems are not unique to pressure-sensitive paint. There has been much research on the effect of surface finish on aircraft drag. A detailed assessment of the drag processes was investigated and documented by *Hoemer* [4.134]. It should be noted that cryogenic testing of a temperature-sensitive paint (TSP) by *Fey* et al. [4.135], with a roughness of < 0.5 µm Ra was accepted by the European transonic wind tunnel (ETW) because this TSP could be polished after spraying and the paint created no additional surface effects like turbulent wedges at the leading edge.

Sources of Error

Bukov et al. [4.129] described many of the errors found in the PSP measurement technique. Typical errors associated with the paint include:

- Nonlinearity of the PSP calibration due to second-order solubility effects requires a second-order fit to reduce errors to 0.2%.
- Spatial variation of the PSP calibration gives a 0.3% error caused by microheterogeneity of the polymerisation. This can be corrected by pixelwise instream calibration in pressurised wind tunnels. This has also been reported by *Torgerson* et al. [4.136] as a more significant error for low-speed flows.
- Temperature sensitivity of the PSP calibration can be a significant error and corrections must be applied. Depending on the PSP dye the error is between 0.3–5%/°C.
- Temperature hysteresis is dependent on the type of polymer used and has been noted by *Jules* et al. [4.137] to be an irreversible effect. Between −20 °C and 80 °C flow or model surface temperature there is no significant error for the DLR02 paint, but for temperatures between 100 °C–120 °C there is also an irreversible effect.
- Pressure hysteresis is caused by the irreversible solubility of oxygen in a polymer and is explained by *Grate* and *Abrahams* [4.138]. Elastic polymers have the lowest hysteresis.
- Spatial resolution is limited by sideways oxygen diffusion in the paint layer, while average time resolution is limited by the paint thickness and diffusion rate. For steady flow using the intensity method this is no problem, but it causes phase errors when measuring dynamic pressure signals.

- Paint ageing. Paints are now more stable than five years ago, when paints could change by as much as 5% per day due to slow polymerisation, slowing down after complete polymerisation. The paint's calibration changes because the environment around the individual dye molecules changes at different rates. This can leave some luminous molecules that are unable to be quenched. The ratio between these insensitive molecules and the sensitive molecules introduces a standing offset in the luminescent signal and changes the linearity of the Stern–Volmer plot [4.139]. In 1996 *Zharkova* et al. [4.109] found that their paint had a very short life and became insensitive to pressure 15 d after spraying. DLR's experience [4.115] using their own DLR02 paint, is that about 10% of sensitivity is lost after half a year storage in a dark box at 20–80% relative humidity at room temperature 20–40 °C.
- Photobleaching is proportional to the intensity of the light source and depends on the type of dye used, and may be significant for some paints.

4.4.3 Imaging Systems

Radiometric Imaging

Radiometric imaging is the simplest and most widely used technique for acquiring pressure-sensitive paint images. The surface is illuminated with a continuous light source and the paint's luminescence is normally detected by a cooled, charge-coupled device (CCD), slow scan camera [4.140].

The Stern–Volmer equation (4.35) predicts that the intensity of the fluorescence is inversely proportional to the partial pressure of oxygen. Equation (4.35) describes the ratio IR of the intensity I of paint at pressure p to the intensity I_0 at zero pressure and has been rewritten as

$$IR = \frac{I}{I_0} = \frac{1}{1+kp}\,, \tag{4.35}$$

where k is the pressure sensitivity of the paint (measurable by calibration).

This equation requires an estimate of the intensity of the paint at zero pressure. This will vary over the surface as the illumination is not uniform and the thickness of the dye on the surface depends on the application method. A wind-off reference image is taken at atmospheric pressure to measure these variations and the Stern–Volmer equation is modified accordingly [4.117]. The pressure image is produced from a ratio between this image and a wind-on image.

Any wind-on model displacement will make direct pixel-by-pixel computation impossible and the registration between the two images has to be corrected by image transformation [4.141]. Various correction methods, also applicable to real three-dimensional wind tunnel models, are developed in most PSP groups.

The error in the illumination intensity (ξ) due to the movement of the model can be approximated by:

$$\zeta \approx \frac{2l^2}{r^2+l^2}\frac{\varepsilon_\mathrm{r}}{r} - \frac{2l^2}{r^2+l^2}\frac{\varepsilon_\mathrm{l}}{l} - \frac{2rl}{r^2+l^2}\Phi\,, \tag{4.36}$$

where r is the distance between the lamp and the model, l is the length of the model, ε_r is the distance of movement from the lamp, ε_l is the distance of movement laterally and Φ is the angular rotation of the model under load.

The most sensitive factor of (4.36) for sting-mounted models is the angular rotation. Sting-bending rotation is corrected by computing the model movement from the measured loads, and pitching the model to the wind-on angle of attack before taking the reference image.

This is quite successful for flat models illuminated using a point source. However, practical light sources tend to deliver a cone of light. This leads to significant changes in illumination over the surface of the model and any model movement will cause pressure measurement errors in the illumination gradient. Highly curved areas of the model, such as leading edges, are similarly affected. The most successful system for correcting for model movement has been demonstrated by *Engler* [4.132, 142]. Here the model attitude and displacement are directly measured and the model is moved by a multidimensional sting actuator to match the reference image to the wind-on image within two pixels. The model is now in the same illumination field for both images. This technique cannot be applied to all wind tunnels. The model deformation can be corrected by the DLR software. The deformation occurs due to the cantilever arrangement of the wings and other surfaces bending under aerodynamic loads.

Lifetime Measurement

Lifetime measurement illuminates the paint with a pulse of light and measures the response with a gated detector. This was one of the first methods [4.101] used to image pressure-sensitive paint with a film camera exposed at various intervals after illumination by a flash lamp. The method has been used to make fluorescence images of microscope slides [4.143] using a scanning laser system and has been adapted for aerodynamics by *Davies* [4.144], *Engler* et al. [4.142] and *Burns* and *Sul-*

livan [4.145]. Figure 4.24 shows the behaviour of the paint when illuminated with a pulse of light. The intensity of the paint J_{pulse} can be modelled, to first order, by an exponential decay:

$$J_{\text{pulse}} = J_0 \exp(-t/\tau) , \tag{4.37}$$

where J_0 is the intensity at time $t = 0$. The lifetime of the paint τ is dependent on pressure in the same way as intensity to first order. Equation (4.19) has been rewritten as

$$\frac{\tau_0}{\tau} = 1 + Kp , \tag{4.38}$$

where τ_0 is the lifetime of the paint at zero pressure and Kp is the pressure sensitivity. Figure 4.24 shows the exponential decay curves for ruthenium- and pyrene-based paints. Since the decay time for ruthenium is in the range 2–10 µs it must be pointed out that for pyrene-based paint the decay time is in the 50–100 ns range and the exponential function is nearly monoexponential. To compute the lifetime at least two measurements of intensity must be made on the decay curve. The measurement of the intensity cannot be performed instantaneous and must be integrated using a time gate (Fig. 4.25). By making the gates the same width t_{gate} (4.37) can be used to predict the relation of the ratio of the two intensities LR to pressure

$$LR = \frac{\int_{t_{\text{gate}}}^{2t_{\text{gate}}} J_{\text{pulse}}\,\mathrm{d}t}{\int_{0}^{t_{\text{gate}}} J_{\text{pulse}}\,\mathrm{d}t} = \exp\left[-(1+Kp)\frac{t_{\text{gate}}}{\tau_0}\right] . \tag{4.39}$$

Often there is no need for a wind-off reference image using this technique. This overcomes the problems associated with model movement and the radiometric method. An experiment by DLR [4.142] gives a good impression of a direct comparison between the intensity and lifetime methods.

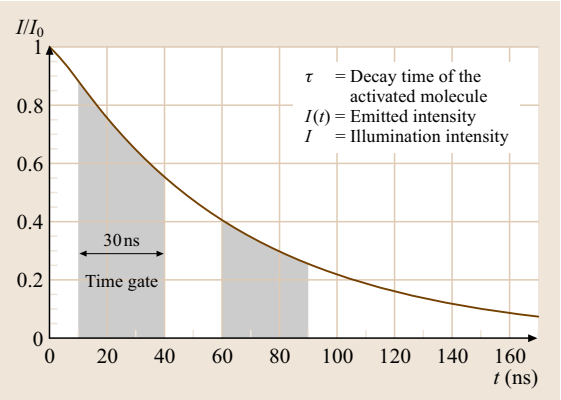

Fig. 4.24 Two-gate technique for pyrene-based paint

Fluorescent Lifetime Imaging

Holmes [4.146] has developed a fluorescent lifetime imaging method which uses a modulated light source to illuminate the paint. He developed an area measurement system based on arrays of light-emitting diodes and a solid-state phase-sensitive camera. The response of the paint can be modelled by using the analogy of a low-pass filter built around a resistor and capacitor. The paint is able to store light in the same way as a capacitor stores charge. The paint emits light in the same way as the capacitor loses charge through the resistor. Because this very specific technique has up to now only be used by him, details can be taken from this report [4.146].

Light Sources

The purpose of a PSP light source is to illuminate the paint at the correct wavelength. The light source must produce sufficient light to enable an image to be taken in a reasonable time frame for the experiment. It is also helpful, but not absolutely necessary, that the light source emits little power in the luminescence band of the paint. Stacks of interference and absorption filters achieve the desired spectrum at the expense of efficiency. The light source must be stable, as any illumination fluctuation is magnified at least four times in the final pressure image.

For paint formulations that require ultraviolet excitation, possible light sources would be based on Hg-vapour

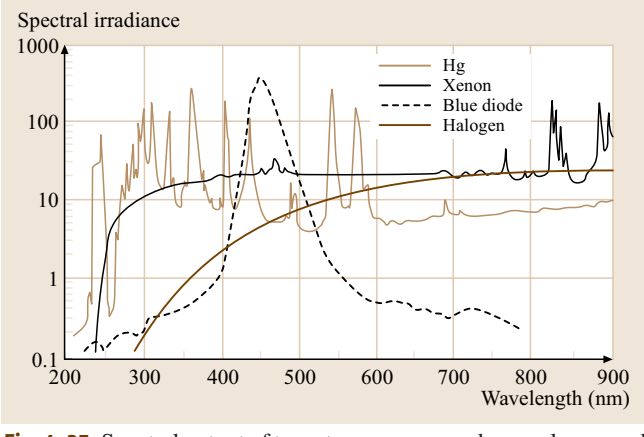

Fig. 4.25 Spectral output of tungsten, mercury and xenon lamps and a blue diode

or xenon-arc lamps, or on an excimer laser. Short-wavelength UV light is not directly visible and is not transmitted by ordinary glass. For paints that are excited in the visible band (usually 400–500 nm), xenon-arc, halogen, argon laser or light-emitting diodes are possible sources (Fig. 4.26).

Laser light sources have obvious benefits in terms of narrow-band, intense illumination. However, lasers have distinct drawbacks as they are heavy, expensive, and must be transported and handled with care. Proper laser safety procedures are essential. The use of lasers requires extensive safety precautions that add complexity to the test schedule. Excimer output energy typically fluctuates less from pulse to pulse. Mirror systems in some designs are sensitive to vibration and temperature change.

Halogen lamps darken less with time than ordinary lamps, but the halogen cycle requires a specific temperature range to operate efficiently. Cooling air circulating around the bulb can block the halogen cycle and shorten the useful life of the lamp. Also, small variations in the operating voltage can have a large effect on the blue end of the spectrum. *Carroll* et al. [4.131] report that a stabilised constant-current power supply can reduce ripple to 0.04%. Optical feedback is often required to improve long-term stability.

The optical output of a mercury-arc or xenon-arc lamp depends on the operating temperature. The lamp must be allowed to achieve thermal equilibrium before taking images, which can take several seconds. Very useful especially for wind tunnels are optical fibers which are directly connected to the arc lamps. Liquid fibers are available for wavelengths from the UV up to the IR, meaning that thermal effects can be reduced to a minimum and electrical problems with high-power devices can also be excluded.

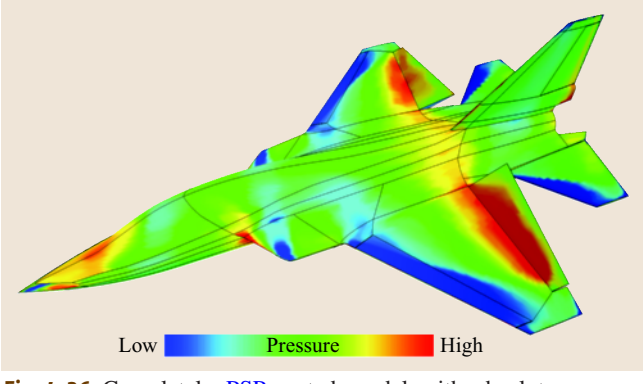

Fig. 4.26 Completely PSP-coated model with absolute pressure distribution to calculate loads

LEDs make excellent light sources for pressure-sensitive paint. Arrays of diodes can be used to illuminate the model from many directions. They are small, easy to mount, produce little heat, and in sufficient numbers they can produce a fairly uniform, tailored, distribution field. Their disadvantage is the change in the emitted wavelengths when they are heated in the wind tunnel, especially in low-speed tunnels where air coolers are not installed.

DLR and THE FRENCH AEROSPACE LAB (ONERA) [4.147] initially used liquid optical fibers, which can be connected to lamps as well as to lasers to transmit the light to the working section. Filters in front of xenon-arc lamps can select the right wavelength for very different paints on the market. From the viewpoint of illumination users are independent of paint selection, because various filter sets can be used.

Detectors

Photographic film was the first detector [4.101] used for pressure-sensitive paint. However the inherent nonlinearity of the emulsions, the sensitivity to processing procedures and the long processing time means that film is seldom used in wind tunnels today. The advantage of photographic film is that it does not require expensive and bulky instrumentation. This has made it the choice for flight trials [4.148, 149].

Wind tunnel researchers use both electronic cameras and scanning detectors to view the paint. Full-field, cooled, scientific-grade, CCD cameras are used for global imaging applications. Photomultipliers and avalanche photodiodes are used for scanning spot applications. Recently phase-sensitive CCD cameras have become available for making global fluorescent lifetime images.

La Belle and *Garvey* [4.150] give an introduction to the properties of CCD cameras suitable for pressure-sensitive paint. CCD cameras come in three varieties: interline, frame-transfer and full-field devices. Interline devices are designed for video picture applications; half of the CCD imaging area is covered by pixels, which slightly reduces their sensitivity and resolution but they have the eminent advantage that they do not need mechanical shutter. After a selected integration time the image will be shifted to the covered area. DLR [4.151] developed in cooperation with the OMT camera company a special black-and-white PSP version of this device for 12- and 14-bit operation. Frame-transfer devices are designed for high frame rates. Full-field devices are designed for scientific imaging applications and are optimised for low-noise operation by slow-

Table 4.2 Observed camera properties

Camera	Run	Median image value	Median intensity ratio	Standard uncertainty	Standard deviation of ratio images
12 bit	1	3780	0.31	0.0019	0.009
16 bit	2	50 063	0.30	0.0008	0.003
Gain = 1	3	13 662	0.299	0.0004	0.0009
Gain = 4	4	10 220	0.284	0.0004	0.0017

ing the scan rate, but they work with a mechanical shutter.

An important factor that controls the use of camera type is the necessity to capture images rapidly in order to increase the run rate and decrease the required tunnel occupancy time. This generated interest in the possibility of trading off analog-to-digital converter (ADC) bit depth for faster image download in the PSP cameras. Therefore signal strength, noise, and measurement uncertainty are compared.

Pressure-sensitive paint (PSP) systems have historically incorporated scientific-grade cameras with 16 bit analog-to-digital converters (ADC). Such high resolution was always considered necessary to resolve small pressure differences, particularly those encountered in low-speed testing. The system has matured such that we now find ourselves conducting more production-oriented tests, with a concomitant requirement to improve overall productivity. A careful accounting of the system revealed a bottleneck in image acquisition caused by the time required to transfer the image data off the camera. This generated an interest in the possibility of trading off ADC bit depth for faster image download.

Exploring this possibility, the specifications of a number of commercially available cameras were collected by *Brown* et al. [4.152], from which their theoretical performance and effective ADC resolution could be compared. The results are shown in Table 4.2. The current standard PSP camera is the Photometrics CH35O^{TM}, shown in the first column. It has an image upload time of 6 s. This compares with times of 2 and 0.12 s for the Photometrics PXL^{TM} camera and the IDT sharpVISION^{TM} 1500EX, which have ADC resolutions of 14 and 12 bits, respectively.

When taking exposures under typical operational conditions, one must also take into account the performance of the charge-coupled devices (CCD). Lower quantum efficiencies will require longer exposure times to accumulate electrons, and higher full-well capacities will require longer times to accumulate maximum signal in order to take full advantage of the ADC resolution. One must also consider the effects of read and shot noise, which reduce the signal-to-noise ratio and can significantly reduce the effective resolution. Taking these factors into account, the effective resolution of the 16 bit Photometrics CH350 camera is actually less than 11 bits, as shown in Table 4.2. The 12 bit resolution of the IDT 1500 is actually a little less than 10. The difference in resolution of these two cameras is more like one or two bits instead of four. Moreover, even though the IDT camera requires almost three times the exposure time of the CH350 camera, its total time per image is less by a factor of six. Perhaps maximum ADC resolution is not optimum, especially considering the high purchase price for high-resolution cameras.

To understand these tradeoffs better, comparative tests were performed on the cameras listed in Table 4.2. Each camera was used to acquire calibration data on a PSP coupon. By using a common coupon, the true performance of each camera in terms of pressure resolution and signal-to-noise ratio could be determined.

Shot noise describes the random variations in accumulating charge in a well of the CCD. This is described by the Poisson probability distribution, which has a standard deviation equal to the square root of the total amount of accumulated charge.

The quantity being accumulated is photons (ph), which are converted to pholoelectrons by the quantum efficiency η, which is then converted to counts by the gain G:

$$\begin{aligned}\sigma_{\text{shot}} &= (\text{ph})^{1/2}\,,\\ \sigma_{\text{shot}} &= (I\eta/G)^{1/2}\eta/G\,,\\ \sigma_{\text{shot}} &= (I\eta/G)^{1/2}\,. \end{aligned} \tag{4.40}$$

In this way, we can estimate the total random uncertainty in a raw image due to read and shot noise as:

$$U_I^2 = \sigma_{\text{read}}^2 + \sigma_{\text{shot}}^2\,. \tag{4.41}$$

Read noise is independent of the signal level, while shot noise increases with the square root of the signal. Using

these equations and the median image values and median intensity ratios, the computed image statistics are shown in Table 4.2.

The uncertainty for the 12 bit camera should be about twice that of the 16 bit camera. The standard deviation of the ratio of the images, showing the data scatter, are represented in Table 4.2.

Noise was estimated by computing the standard deviation of the residuals, that is, the differences between the pixel data and the least-squares line. The signal level was quantified by computing the range of the least-squares line, namely the maximum minus the minimum value. The results are shown in Table 4.3.

The variation in intensity ratio across the coupon is on the order of 0.01. For this signal level, the 12 bit camera has a signal-to-noise ratio of 1, while the 16 bit camera has a signal-to-noise ratio of 6. Looking at it in another way, the 12 bit camera has an observed noise level of 0.009 in intensity ratio, which corresponds to 0.16 psi. The 16 bit camera has an observed noise level of 0.002 in intensity ratio, corresponding to 0.037 psi. The 12 bit IDT camera can discern pressure variations that are only four times larger than we can currently see with the 16 bit CH350 camera.

With the gain set to 1, the PXL camera has an observed noise level of 0.0007 in intensity ratio, which corresponds to 0.0013 psi. When the gain is set to 4, the observed noise level is increased to 0.0014, corresponding to 0.023 psi. The PXL camera can discern smaller pressure variations when the gain is set to 1 than 4.

The 12 bit camera should not replace the 16 bit camera. The resolution of the 12 bit camera is not high enough to discern actual fluctuations on the order of 0–2 psi. The random uncertainty due to read and shot noise is also up to three times as high for the 12 bit camera and the signal is lost in the noise.

The impact of gain on the PXL cameras has been quantified. These cameras should be used with the gain set to 1, because they have a higher signal-to-noise ratio and the camera can discern smaller pressure fluctuations.

Table 4.3 Camera signal properties

Camera	Run	Signal	$S_{residual}$	S/N ratio
12 bit	1	0.0098	0.0085	1.2
16 bit	2	0.0104	0.0017	6.3
Gain = 1	3	0.0013	0.0007	1.9
Gain = 4	4	0.0013	0.0014	0.9

Filters

Light filters are used to separate the luminescence from the excitation light source. Filters can be split into two categories:

- *Interference filters* select a band of light through a complex process of constructive and destructive interference. They consist of a substrate onto which varying thicknesses and types of chemical layers are vacuum deposited in such a fashion that the transmission of certain wavelengths is enhanced, while other wavelengths are either reflected or absorbed. *Bandpass filters* only transmit light in a defined spectral band. The peak central wavelength and spectral width can be controlled very tightly. *Edge filters* only transmit light above (long pass) or below (short pass) a certain wavelength. They are designed to exhibit a sharp transition over a narrow wavelength range and are frequently known as *hot* and *cold mirrors*. Short-pass filters tend to only have a limited stop band and also transmit long wavelengths.
- *Colour glass filters* are used for applications that do not need precise control over wavelengths and transmission intensities. They operate by selective absorption within the glass to give different spectral characteristics and are relatively inexpensive compared to interference filters.

The key filter characteristic is the ratio of transmission to blocking. The integral over wavelength is computed to compare different filters.

Filters may not be operated above 60 °C and must be cooled to remove the heat caused by the incident and absorbed radiation. All filters are sensitive to the angle of incidence of the incoming light. For interference filters the peak transmission wavelength will decrease for angles away from normal, while the bandwidth and transmission characteristics generally remain unchanged. For colour glass filters increasing the incidence angle increases the transmission path, reducing the transmission efficiency.

Excitation light sources require short-pass filters. Researchers often use a stack of filters to first remove the IR spectrum then block the spectral region of the paint luminescence. Bandpass filters tend to be used on the detector to block the excitation light source.

4.4.4 Processing

All pressure-sensitive paint results are generated from two or more measurements or images. The form of

the processing is highly dependent on the experimental method. *Stilwell Bowen* [4.153] recommends that any data-reduction methodology should be user independent. The following processes are often performed on the pressure data.

Remove Self-Illumination Effects

Self-illumination is the reflectance of luminescence from one part of a model to another. It can occur on complex model structures. The signal from any point on the model is the sum of all the rays reflected from other points. *Bukov* et al. [4.129] found that associated pressure errors can be as large as 8% without correction. This forced them to test individual components separately. *Ruyten* describes the processing involved to make these corrections [4.154]. *Engler* et al. [4.151] found that in the most cases the typical error produced by analysing the models in parts is about 3%, but the influence of the test section with its windows and polished walls can create an additional 3–6% error. Therefore it is recommended to cover the test section with absorbing paint or self-adhesive layers, as done by these authors in various wind tunnels with great success.

Calibration

Three types of pressure calibration are routinely performed for pressure-sensitive paint:

- A priori methods either calibrate a coupon of paint or the complete model in a pressure chamber.
- In situ calibration uses the pressure-sensitive paint to interpolate between pressure taps.
- Direct calibration of the complete model in the wind tunnels test section, which is only possible when the tunnel can be pressurised.

The advantage of a priori calibration is that the paint is a standalone transducer that can be used on any model. However, the absolute level of pressure can be difficult to compute due to the many bias errors that affect the measurement. *Engler* [4.132] achieved an accuracy of ±1 mbar for a paint calibrated externally and for the same paint calibrated by changing the pressure of the tunnel without flow. *Engler* [4.132] controlled the temperature to ensure that thermal errors were reduced by using the paint at its minimum sensitivity.

Mebarki [4.155] proposed a general formulation of the Stern–Volmer law where the calibration coefficients are temperature dependent. This a priori allows different temperature conditions to be taken into account between the reference and the wind-on measurements.

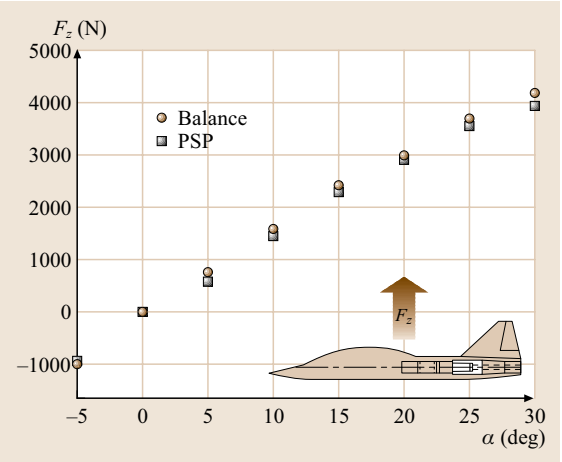

Fig. 4.27 Comparison of normal forces F_z (PSP and balance)

The major sources of bias errors in all calibrations are thermal and illumination errors. These have forced many researchers to apply different calibrations to separate parts of the model. This makes the data-reduction process very user dependent and no longer traceable.

Analysis

Most researchers present their data as calibrated pressure images and chord-wise distributions compared to pressure taps. DLR [4.151] have presented real 360° PSP results from the transonic wind tunnel HST (High Speed Windtunnel) of DNW (Deutsch/Niederländischer Windkanal) at Amsterdam (Fig. 4.27). Three-dimensional

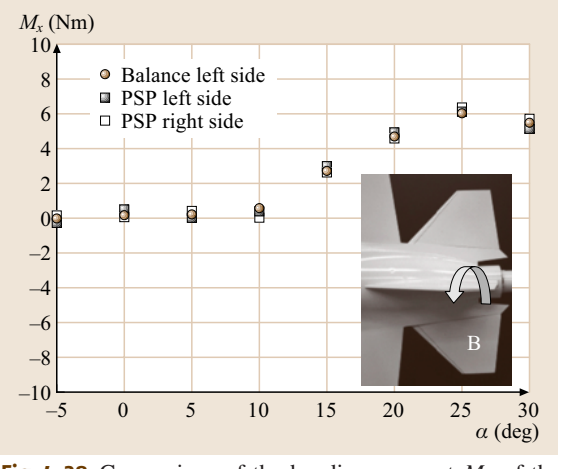

Fig. 4.28 Comparison of the bending moment M_x of the model (PSP and balance)

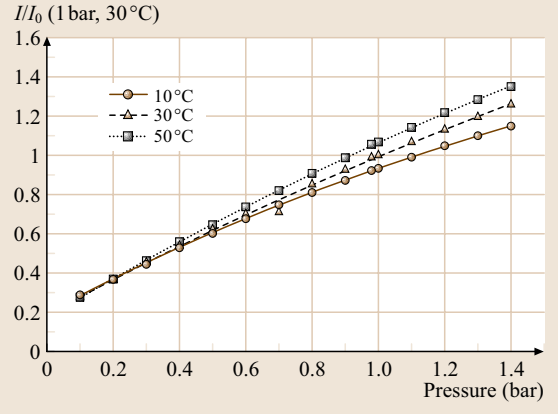

Fig. 4.29 Typical intensity calibration for a pressure-sensitive paint

wind-tunnel models showing the pressure distribution were obtained by pressure-sensitive paint using eight cameras simultaneously. The complete pressure integration around the model surface gives the loads. However, detailed comparison with internal balances shows the accuracy which is possible today.

The goal for industrial pressure-sensitive paint is to produce fully qualified, traceable pressure data in a form suitable for input into aircraft design procedures. For the measurements of Fig. 4.27 a structured grid was used to transform the results from pixel values to the knot points of the grid. For each knot point the coordinates x, y, z and C_p value exist for the complete model. All data were given to the clients in ASCII as well as Tecplot format.

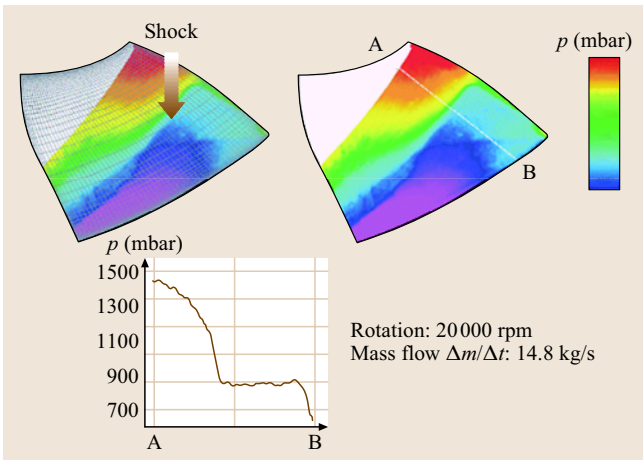

Fig. 4.30 Pressure distribution on a turbine blade

The pressure maps were used for later integration to calculate the total loads of the model (Fig. 4.28) and of single components like the horizontal tail (as shown in Fig. 4.29). The main goal of this test was to obtain detailed information about the accuracy of the PSP data.

The PSP method can be an excellent tool to detect the sources of separation on the model's surface, because balances give information averaged over the complete model, or model parts equipped with balances.

Asymmetric pressure distributions on the wings as obtained by means of PSP made these effects obvious. As far as the quantitative data are concerned the difference between hinge moment balances and PSP is about $\approx 5\%$ in moments for symmetric flow using lenses with a large zoom factor (Fig. 4.29). Online PSP data [4.151] provide a fast overview of the pressure field over the very wide flight envelope of the aircraft, both in terms of speed and angle of attack. This helps reduce the effort, costs and time required for numerical calculations of the pressure field and the loads considerably.

Thermal Compensation

Figure 4.30 shows a typical pressure and temperature calibration for a pressure-sensitive paint, where thermal effects can be seen. The main problem with any thermal correction technique is that the precision of the temperature measurement must be accurate enough that the correction process does not introduce errors into the pressure measurement.

This problem has yet to be adequately solved. *Morris* and *Donovan* [4.156] used a temperature-sensitive paint to generate a thermal map to compensate the pressure-sensitive paint. The two paints were applied and data acquired in separate runs. This technique has been particularly useful in the visualisation of turbine blades as separate blades can be sprayed and the data acquired in the same run.

Researchers have succeeded in combining two dyes in the same binder to make pressure and temperature measurements [4.157]. This method will probably yield the best results as both dyes are in close proximity to one an other and should be at the same temperature. *Henne* [4.119] realised this and used infrared thermography images to correct for thermal errors in the pressure-sensitive paint method.

4.4.5 Applications

Subsonic–Transonic Flow

There have been numerous papers written on the use of pressure-sensitive paint in flows between Mach = 0.4

and 1.4. Error analysis predicts that this is probably the flow regime where pressure-sensitive paint is the most effective due to the large changes in pressure and relatively small thermal effects. This flow regime also matches the envelope of many military and civil models in industrial wind tunnels. Pressure-sensitive paint is expected to reduce aircraft development costs by reducing the manufacturing costs and time. Most major developers have now conducted trials using pressure-sensitive paint, although many do not publish the results due to customer confidentiality [4.81–98, 158–175].

Supersonic Flow

Some of the first pressure-sensitive paint results [4.101] were made at Mach = 3.0 on a sphere, a blunt cone and a wedge. Thermal errors were kept to a minimum by choosing paint with a low thermal sensitivity in the temperature range of the experiment.

Early work by *Morris* et al. [4.140] showed that their paints adhered to the model in the regions of highest shear stress in a Mach = 2.0 flow, even though the paint could be damaged by touch. *McLachlan* et al. [4.157] gave a detailed account of a test at Mach = 1.6–2.0. The thermal errors meant that an a priori calibration could not be used, as the temperature was not measured. The best accuracy of 0.017 C_p was achieved by only computing pressure values for single chord lines and using in situ calibration at this time.

Paints were developed at DLR for tests up to Ma = 6.0 for temperatures between −40 °C and +80 °C. These paints resist all the demanding conditions of such a flow, although condensation remains a problem, as the quenching process is constrained and does not then give correct pressure results.

Hypersonic Flow

Borovoy et al. [4.133] published the results of their findings at Mach = 6.0 and 19–74 bar in a shock wind tunnel with a 40 ms run time. At these speeds thermal effects cause the greatest errors.

Images were taken 8–18 ms after the start of a run so that the paint had time to react to pressure changes, but before thermal changes affected the paint characteristics. The PSP results were within 10% of the prediction when compared to computational fluid dynamics (CFD).

Jules et al. [4.137] also reported that thermal errors significantly affected the response of paints tested in the hypersonic regime. They found that beyond a certain temperature threshold the paint intensity degradation became irreversible. *Morris* and *Donovan* [4.156] used a temperature-sensitive paint in a separate run to measure the surface temperature of the model and correct the pressure results.

Low-Speed Flow

Pressure-sensitive paint is an absolute pressure transducer and is not suited to low-range differential pressures. Performance can only be improved by increasing the precision of the measuring instrument. For CCD cameras this equates to reducing the shot noise, which requires averaging sequences of images. *Sajben* [4.176] showed theoretically that C_p measurement errors increase at low Mach numbers due to the small pressure differences generated. However, *Morris* et al. [4.177] have shown that low-speed measurements are possible by careful experiment design. Valid pressure measurements have been obtained at 20 m/s on a NACA 00 12 airfoil model with an error of 0.12 in C_p [4.178].

Torgerson et al. [4.136] managed a pressure resolution of 0.01 psi. They found that model movement gave significant errors and used two-dye paints and phase-sensitive laser scanning to remove the need for reference images. They were also limited by spatial variations of the paint characteristic caused by the microheterogeneity of the polymer structure.

Verhaagen [4.179] used pressure-sensitive paint to compare the vortex structure on a double delta wing to CFD predictions.

In the paper by *Engler* [4.180] describing cooperative work between DLR and ONERA various tests are described from car investigations with the advantage of a hard-shell model (no distortion between wind-off and wind-on image) to obtain high-pressure resolution. They also describe the tests as low speed, but the main problem is temperature correction, because normal low-speed wind tunnels have no coolers and the temperature changes during the runtime of a complete set of a alpha-polar requires about 30 min and already creates temperature changes of up to 20 °C. *Henne* [4.119] solved this problem using infrared cameras for pixel-by-pixel temperature correction.

Turbine Measurement

The measurement of pressures on turbine blades has traditionally been difficult. The use of pressure-sensitive paint offers a potential solution but there are problems that need to be solved. These include: poor optical access, large thermal gradients, the need to *freeze* rapidly moving blades and the problems of generating reference images. There appear to be few papers published

in the open literature, but several outstanding experiments were presented at the Fifth Pressure-Sensitive Paint Workshop held at Arnold Engineering Development Center (AEDC), USA in May 1997.

It is also known that TsAGI have made significant advances measuring rotating machinery [4.181]. *Trinks* [4.182] investigated the shock location on turbomachines as a function of the mass flow. The rotation of the blades was 20 000 rpm at a temperature of about 40 °C.

Two-dimensional flow measurements have been made on the end wall of a cascade wind tunnel. *Burns* and *Sullivan* [4.145] used a scanning laser to excite PSP on a fan blade. A photomultiplier tube detected the paint decay and the pressure was computed by a lifetime measurement.

In Flight

McLachlan et al. [4.118] imaged, from the inside, the pressure distribution of a pressure plotted window coated with a UV-excited paint. The experiment was self-contained and mounted under an F-104G aircraft flying between Mach = 1.0 and 1.6. A standard 8 bit video camera was used. The experiment had to be done at night to minimise ambient light intrusion. An in situ calibration was used due to avoid photodegradation. An accuracy of 35 psf in the range of 400 psf was achieved at Mach = 1.6. At Mach = 1.3 thermal effects dominated the results.

Houck et al. [4.148] conducted a flight test to image the pressure distribution on a practice bomb coated with a blue-light-excited paint. The experiment used a conventional film camera and custom flash light sources as a self-contained unit attached to an adjacent aircraft hard point. The film was processed and digitised by projection onto a scientific-grade CCD camera. Luminescent reference markers were used to correct for illumination fluctuation.

Unsteady Measurements

Investigations of unsteady processes are becoming increasingly important in aerodynamic. A large amount of experience exists for steady measurements, but the industry and some aerodynamic areas such as aeroelasticity and turbomachinery need new, fast measurement techniques like the nonintrusive and planar PSP method, also to optimise their own CFD calculations. The first steps in paint development have been taken, with short response times in the region of 0.1 ms to 50 µs.

Winslow et al. [4.113] analysed the response time of a PSP luminescence which obeys a linear Stern–Volmer relation. According to their theory, the time to reach 90% of the total response is:

$$t_{90\%} = 0.85\frac{h^2}{D}\,, \tag{4.42}$$

where h denotes the thickness of the PSP layer and D the gas diffusivity in the layer. The flow in the micropore is close to free-molecular flow, because the diameter of the micropore in the anodised aluminum is less than the mean free path of gas molecules. The diffusion process in such a case is called Knudsen diffusion. The gas diffusivity of the Knudsen diffusion is

$$D = d\sqrt{\frac{8RT}{9\pi}}\,, \tag{4.43}$$

where d denotes the pore diameter, R the gas constant for a unit mass, T the absolute temperature, and π the ratio of the circumference of a circle to its diameter. The gas constant for air is 287 J/(kg K). Note that the diffusion coefficient is linearly proportional to d.

The response of the hydrophobic AA-PSP to a step change in pressure was tested by using a shock tube. Such a shock tube can produce a sharp, discontinuous pressure change (normal shock) with a rise time of less than a microsecond. The PSP sample was placed at the end of the tube. A photomultiplier tube was used to measure the luminescent intensity.

In terms of the hardware, the main problem is still data acquisition using fast complementary metal oxide semiconductor (CMOS) CCD cameras and fast data storage. The first steps have mainly been made in paint development. After the successful development of *conventional* PSP, industrial partners are now encouraging the investigation of these more-complex problems.

4.4.6 Concluding Remarks

Pressure-sensitive paints have been developed since the early 1980s. A number of theoretical concepts are involved, but in the late 1990s the technique reached sufficient maturity to be used as a tool in industrial wind tunnels.

Pressure-sensitive paint is an absolute transducer that converts a unit of pressure into a unit of light. The paint can be calibrated in situ or a priori. There are several methods to acquire the data: radiometric, lifetime and fluorescent lifetime imaging etc.. The raw data requires image processing to produce pressure results.

Optical pressure measurement has been used in production testing for subsonic and supersonic up to cryogenic flows [4.183–187]. Developers are beginning to solve the problems involved in low-speed and hypersonic applications. Satisfactory thermal compensation techniques are in progress but data reduction is still very user dependent.

The goal for industrial pressure-sensitive paint is to produce fully qualified, traceable pressure data in a form suitable for input into aircraft design procedures.

References

4.1 D.W. Bryer, R.C. Pankhurst: *Pressure Probe Methods for Determining Wind Speed and Flow Direction*, Technical Report (Her Majesty's Stationery Office, London 1971), .

4.2 S.H. Chue: Pressure probes for fluid measurement, Prog. Aerosp. Sci. **16**, 147–223 (1975)

4.3 A. Thom, C.J. Appelt: The pressure in a two-dimensional static hole at low Reynolds numbers, Rep. Memor. Aero. Res. Council **3090** (1957)

4.4 R.E. Rayle Jr.: An investigation of the influence of orifice geometry on static pressure measurements, MS Thesis (M.I.T., Boston 1949)

4.5 C.M. Allen, L.J. Hooper: Piezometer investigation, ASME Trans. **54**(HYD-54-1) (1932)

4.6 C. Ducruet, A. Dyment: The pressure-hole problem, J. Fluid Mech. **142**, 251–267 (1984)

4.7 J.L. Livesey, J.D. Jackson, C.J. Southern: The static-hole error problem: an experimental investigation of errors for holes of varying diameters and depths, Aircraft Eng. **34**, 43–47 (1962)

4.8 R. Shaw: The influence of hole dimensions on static pressure measurements, J. Fluid Mech. **7**, 550–564 (1960)

4.9 A. Miyadzu: Über den Einfluss der Bohrungen auf die Druckanzeige, Ingen.-Arch. **7**, 35–41 (1936), in German

4.10 A.K. Ray: On the effect of orifice size on static pressure reading at different Reynolds numbers, Ing.-Arch. **24**(3) (1956), , Engl. transl. Aero. Res. Counc. unclassified 'A3' report 18829, FM 2479, EA 527, TP 498

4.11 R.E. Franklin, J.M. Wallace: Absolute measurements of static-hole error using flush transducers, J. Fluid Mech. **42**, 33–48 (1970)

4.12 G. Fuhrmann: Theoretische und experimentelle Untersuchungen an Ballonmodellen, Ph.D. Thesis (Göttingen University, Göttingen 1912)

4.13 B.J. McKeon, A.J. Smits: Static pressure correction in high Reynolds number fully developed turbulent pipe flow, Meas. Sci. Tech. **13**, 1608–1614 (2002)

4.14 W. J. Rainbird: Errors in measurement of mean static pressure of a moving fluid due to pressure holes. In: Quart. Bull. Div. Mech. Eng. Nat. Aero. Est. DME/NAE #3, (Nat. Res. Council, Ottawa, 1967)

4.15 E.B. Plentovich: Status of orifice induced pressure error studies, AIAA **84-0245** (1984)

4.16 C. Ducruet: A method for correcting wall pressure measurements in subsonic compressible flow, J. Fluids Eng. **113**, 256–260 (1991)

4.17 M.V. Zagarola: Mean-flow scaling of turbulent pipe flow, Ph.D. Thesis (Princeton University, Princeton 1996)

4.18 V.A. Sandborn: *Experimental evaluation of momentum terms in turbulent pipe flow*, Tech. Note, Vol. 3266 (NACA Lewis Flight Prop. Lab., Cleveland 1955)

4.19 G.K. Patterson, W.J. Ewbank, V.A. Sandborn: Radial pressure gradient in turbulent pipe flow, Phys. Fluids **10** (1967)

4.20 T. Christiansen, P. Bradshaw: Effect of turbulence on pressure probes, J. Phys. E **14**, 992–997 (1981)

4.21 A. Pope, J.J. Harper: *Low-speed Wind Tunnel Testing* (Wiley, New York 1966)

4.22 H.W. Liepmann, A. Roshko: *Elements of Gas Dynamics* (Wiley, New York 1957)

4.23 S. Goldstein: A note on the measurement of total head and static pressure in a turbulent stream, Proc. Roy. Soc. London A **155**(886), 570–575 (1936)

4.24 A. Fage: On the static pressure in fully-developed turbulent flows, Proc. Roy. Soc. A **155**(886), 576–596 (1936)

4.25 P. Bradshaw, D.G. Goodman: The effect of turbulence on static-pressure tubes, Rep. Memor Aero. Res. Council **3527** (1968)

4.26 B.L. Welsh, P.R. Ashill: *Pressure Measurement Techniques in Use at the Royal Aerospace Establishment*, von Karman Institute Lecture Series (1989)

4.27 R.H. Engler, K. Hartmann, B. Schulze: A new optical pressure measurement system (OPMS) ICIASF' 91 Record, Rockville (1991) pp. 163–170

4.28 O.S. Wolfbeis, M.J.P. Leiner: Recent progress in optical oxygen sensing, SPIE Proc. **906**, 42–48 (1988)

4.29 A. Baron, M. Gouterman: 100 µs images of unsteady surface flow using fast responding pressure sensitive paint, Proc. 7th Int. Symp. Flow Visualization, Seattle (1995)

4.30 D. Lubbers, N. Opitz: Quantitative fluorescence photometry with biological fluids and gases, Adv. Exp. Med. Bin. **75**, 441–448 (1976)

4.31 M. P. Gouterman, I. L. Kavandi, J. Gallery, J. B. Callis: Surface pressure measurement by oxygen quenching of luminescence, European Patent Application 0 472 243 A2, August (1991)

4.32 K. Asai, H. Kanda, J.P. Sullivan: Boundary layer transition detection in a cryogenic wind tunnel using luminescent paint, J. Aircraft **34**(I), 34–42 (1997)

4.33 J. H. Bell, B. G. McLachlan: Image registration for luminescent paint sensors, ALAA J. (1993) paper 93–0178

4.34 A. Orlov, V. Radchenko, N. Sadovskii, I. Truyanovsky: Luminescent pressure sensitive composition, European Patent Application 0 558 771 AI, March (1992)

4.35 Y. Mebarki, M. C. Merienne, Y. Le Sant: Application d'un revetement luminescent a deux composes pour la mesure de lapression et de la temperature, Societe Francais des Thermiciens (SFT), Journee d'Etudes (1997)

4.36 J.R. Lakowicz, et al.: Fluorescent lifetime imaging, Anal. Biochem. **202**, 316–330 (1992)

4.37 C. G. Morgan: Measurement of luminescence, US Patent 5,459,323 (1995)

4.38 D. M. Oglesby, C. K. Puram, B. T. Upchurch: Optimisation of measurements with pressure sensitive paints, NASA TM (4695), June (1995)

4.39 A. P. Bukov, et al.: Application of luminescent quenching for pressure field measurements on the model surface, Proc. Wind Tunnels Wind Tunnel Test Tech. Conf., Royal Aeronautical Society, Southampton (1992)

4.40 T. Araki, H. Misawa: Light emitting diode–based nanosecond ultraviolet light source for fluorescence lifetime measurements, Rev. Sci. Inst. **66**, 2 (1995)

4.41 Y. Le Sant, M–C. Merienne: An image resection method applied to mapping techniques, IEEE ICIASF Record Wright–Patterson AFB, 46.1–46.8 (1995)

4.42 J. W. Holmes: Fluorescent lifetime imaging for pressure sensitive paint, GARTEUR AD(AG–21) Final Report, HWA/CN/RD/98006/1 (1998)

4.43 R.M. Dowgwillo, M.J. Morris, J.F. Donovan, M.E. Benne: Pressure sensitive paint in transonic wind–tunnel testing of the F–15, J. Aircraft **33**, 1 (1996)

4.44 R. M. Dowgwillo, et al.: The application of the pressure sensitive paint technique to high speed wind tunnel testing of a fighter aircraft configuration with complex store loadings, AIAA J. (1994) paper 94–1932

4.45 J. P. Crowder: Flow visualisation in flight testing, AIAA J. 90–1273 5th Biannual Flight Testing Conference (1990)

4.46 R. H. Engler, K. Hartmann, I. Troyanovski, A. Vollan: Description and assessment of a new optical pressure measurement system (OPMS) demonstrated in the high speed wind tunnel of DLR in Göttingen, DLR-FB 92-24, 1–66 (1992)

4.47 M.C. Merienne, Y. Mebarki: Contribution to the study of wing–nacelle interaction, Proc. CEAS Wind Tunnels and Wind Tunnel Test Tech. Conf., Cambridge (1997)

4.48 M. Kammeyer, C. Kelble, J. Donovan, M. Benne, T. Kihlken: Recent improvements in pressure–sensitive paint measurement accuracy at, Boeing, AIAA 2002–2907, 22nd AIAA Aerodynamic Measurement Technology and Ground Test Conference, St. Louis (2002)

4.49 M. Kammeyer, J. Donovan, C. Kelble, M. Benne, T. Kifilken, J. Felter: Accuracy assessment of a pressure–sensitive paint measurement system, AIAA 2002–0530, 40th AIAA Aerospace Sciences Meeting and Exhibit, Reno (2002)

4.50 T. Gadella, T. Jovin, R. Cegg: Fluorescence lifetime imaging microscopy (FLIM): Spatial resolution of microstructures on the nanosecond time scale, J. Biophys. Chem. **48**, 221–239 (1993)

4.51 C. Klein: Einsatz einer druckempfindlichen Beschichtung (PSP) zur Bestimmung des momentanen Druckfeldes von Modellen im Windkanal. Dissertation (University Göttingen), DLR-Forschungsbericht 97–55 (1997)

4.52 R.H. Engler, M.C. Merienne, C. Klein, Y. Le Sant: Application of PSP in low speed flows, Aerosp. Sci. Technol. **6**, 313–322 (2002), DLR Göttingen and ONERA Meudon (2002)

4.53 Y. Iijima, Y. Egami, A. Nishizawa, K. Asai, U. Fey, R. H. Engler: Optimization of temperature-sensitive paint formulation for large-scale cryogenic wind tunnels, 20th ICIASF'03 Record, Göttingen, (2003) 70–76

4.54 H. Sakaue, J.W. Gregory, J.P. Sullivan, S. Raghu: Porous pressure sensitive paint for characterizing unsteady flowfields, AIAA J. **40**, 1094–1098 (2002)

4.55 K. Asai, H. Kanda, C. T. Cunningham, R. Erausquin, J. P. Sullivan: Surface pressure measurement in a cryogenic wind tunnel by using luminescent coating, International Congress on Instrumentation in Aerospace Simulation Facilities '97 Record (1997) pp. 105–114

4.56 Y. Amao, K. Asai, I. Okura: Photoluminescent oxygen sensing using palladium tetrakis(4-carboxyphenyl)porphyrin self-assembled membrane on alumina, Anal. Commun. **36**, 170–180 (1999)

4.57 M. Kameda, N. Tezuka, T. Hangai, K. Asai, K. Nakakita, Y. Amao: Adsorptive pressure-sensitive coatings on porous anodized aluminium, Meas. Sci. Technol. **15**, 489–500 (2004)

4.58 V. Mosharov, V. Radchenko, A. Orlov: Binary pressure paint: A lot of problems, Presented at the 7th Annual Pressure Sensitive Paint Workshop, Purdue Univeristy, West Lafayette (1999)

4.59 R. H. Engler: Development of pressure sensitive paint, Presented at the 7th Annual Pressure SensitivePaint Workshop, Purdue Univeristy, West Lafayette (1999)

4.60 J. Crafton, S. Fonov, E. Jones, L. Goss, C. Carter: Bi-luminophore pressure-sensitive paint development, 8th Annual Pressure Sensitive Paint Workshop, NASA Langley Research Center (2000)

4.61 M. Kameda, T. Tabei, K. Nakakita, H. Sakaue, K. Asai: Image measurements of unsteady pressure fluctuation by a pressure-sensitive coating on porous anodized aluminum, Meas. Sci. Technol. (2005)

4.62 J. W. Gregory: Porous pressure-sensitive paint for measurement of unsteady pressures in turbomachinery, Proc. 42nd AIAA Aerospace Sci. Meeting Exhibit, AIAA-2004 294 (2004)

4.63 Y. Sakamura, M. Matsumoto, T. Suzuki: High frame-rate imaging of surface pressure distribution using a porous pressure-sensitive paint, Meas. Sci. Technol. **16**, 759–765 (2005)

4.64 T. Kawakami, T. Tabei, M. Kameda, K. Nakakita, K. Asai: Unsteady pressure-field measurements by a fast-responding PSP on porous anodized aluminum, Proc. 11th Int. Symp. Flow Visualization (2004) Paper No. 217

4.65 H. Sakaue, T. Tabei, M. Kameda: Hydrophobic monolayer coating on anodized aluminum pressure-sensitive paint, Sens. Actuat. (2005) (in preparation)

4.66 H. Masuda, K. Fukuda: Ordered metal nanohole arrays made by a two-step replication of honeycomb structures of anodic alumina, Science **268**, 1466–1468 (1995)

4.67 H. Masuda, F. Hasegawa, S. Ono: Self-ordering of cell arrangement of anodic porous alumina formed in sulfuric acid solution, J. Electrochem. Soc. **144**, L127–L130 (1997)

4.68 H. Masuda, K. Yada, A. Osaka: Self-ordering of cell configuration of anodic porous alumina with large-size pores in phosphoric acid solution, Jpn. J. Appl. Phys. **37**, L1340–L1342 (1998)

4.69 M. Saito, Y. Shiga, M. Miyagi, K. Wada, S. Ono: Optical transmittance of anodically oxidized aluminum alloy, Jpn. J. Appl. Phys. **34**, 3134–3138 (1995)

4.70 T. Hangai, M. Kameda, K. Nakakita, K. Asai: Time response characteristics of pyrene-based pressure-sensitive coatings on anodic porous alumina, Proc. 10th Int. Symp. Flow Visualization (2002) Paper No. F0269

4.71 I. Gursul: Recent development in delta wing aerodynamics, Aeronautical J. **108**, 437–452 (2004)

4.72 D.G. Mabey: Some aspects of aircraft dynamic loads due to flow separation, Prog. Aerospace Sci. **26**, 115–151 (1989)

4.73 N. Chandrasekharan, M. Hammer, L. Kelly, L. A. Mattes: A paradigm shift for pressure sensitive paints, The 8th Pressure Sensitive Paint Workshop, NASA Langley Research Center (2000)

4.74 Y. Sakamura, Y. Kidoh, T. Suzuki, M. Matsumoto: Time resolved pressure measurements in shock-induced flows usinga pressure-sensitive paint, Proc. 23rd Int. Symp. Shock Waves, Fort Worth (2001) pp. 456–462

4.75 R. Crites, M. Benne: Emerging technology for pressure measurements in wind tunnels – pressure sensitive paint, AIAA 95–0106, Presented at the 33rd Aerospace Sciences Meeting, Reno (1995)

4.76 J. H. Bell: Accuracy limitation of lifetime-based pressure sensitive paint measurements, 19th Int. Congr. Instrum. Aerospace Simulation Facilities, Cleveland (2001)

4.77 L. P. Goss, D. D. Trump, B. Sarka, L. N. Lydick, W. M. Baker: Multi-dimensional time-resolved pressure-sensitive-paint techniques: A numerical and experimental comparison, AIAA-2000–0832, Presented at the 38th Aerospace Sciences Meeting, Reno (2000)

4.78 T. Liu, S. D. Torgerson, J. P. Sullivan, R. Johnston, S. Fleeter: Rotor blade pressure measurement in a high speed axial compressor using pressure and temperature sensitive paints, AIAA-97–0162, Presented at the 35th Aerospace Sciences Meeting, Reno (1997)

4.79 A. G. Davies: Temperature compensated PSP measurements on a 2D wing in transonic flow, Presented at the 6th Pressure-Sensitive Paint Workshop, Seattle (1998)

4.80 J.W. Holmes: Analysis of radiometric, lifetime and fluorescent lifetime imaging for pressure sensitive paint, Aeronaut. J. **2306**, 189–94 (1998)

4.81 W. M. Baker: Recent experiences with pressure sensitive paint testing AIAA-2001–0306, Presented at the 39th Aerospace Sciences Meeting, Reno (2001)

4.82 M. E. Sellers: Application of pressure sensitive paint for determining aerodynamic loads on a scale model of the F-16C AIAA-2000–2528, Presented at the 21st Aerodynamic Measurement Technology and Ground Testing Conference, Denver (2000)

4.83 W.M. Ruyten: Self-Illumination Calibration Technique for Luminescent Paint measurements, Rev. Sci. Instrum. **68**(7), 3452–57 (1997)

4.84 S. Ponomarov, M. Gouterman: Ideality of Pressure-Sensitive Paint, I. Platinum Tetra(penta-fluorophenyl)porphine in Fluoroacrylic Polymer, J. Appl. Polym. Sci. **77**(8), 2795 (2000)

4.85 M. Lyonnet, B. Deleglise, G. Grenat, A. Bykov, V. Mosharov: The two-component PSP investigation on a civil aircraft model in S2MA wind tunnel, AGARD Conf. Proc. CP-601: Adv. Aerodyn. Meas. Technol., 81st Fluid Dyn. Panel Sym, Seattle, pp 30–1 – 30–8. Neuilly -sur-Seine, France: AGARD (1998)

4.86 V. Mosharov, V. Radchenko, S. Fonov: Luminescent pressure sensors in aerodynamic experiment, Moscow: Cent. Aerohydrodyn. Inst. (TsAGI). CWA Int. Corp. (1997) p. 151

4.87 T. Liu, B.T. Campbell, S.P. Burns, J.P. Sullivan: Temperature- and pressure-sensitive luminescent paints in aerodynamics, Appl. Mech. Rev. **50**(4), 227–246 (1997)

4.88 K. Nakakita, M. Kurita, K. Mitsuo: Development of the pressure-sensitive paint measurement for large wind tunnels at japan aerospace exploration agency, 24th Congress of the International Council of the Aeronautical Sciences, Yokohama (2004) ICAS2004–3.2.2

4.89 J. H. Bell: Applications of pressure sensitive paint to testing at very low flow speeds, 42nd AIAA.

Aerospace Sciences Meeting & Exhibit, Reno (2004) AIAA-2004-0878
4.90 K. Mitsuo, Y. Iijima, A. Nishizawa, K. Nakakita, K. Asai: Application of PSP. Measurement to low speed wind tunnel testing using an automobile model, Proc. MOSAIC Workshop, Tokyo (2003) pp.70–71
4.91 Y. Mébarki, K. R. Cooper: Aerodynamic testing of a generic automotive model with pressure sensitive paint, 10th Int. Symp. Flow Visualization, Kyoto (2002) ISFV-2002-F0120
4.92 Y. Le Sant, F. Bouvier, M. C Merienne, J. L Peron: Low speed tests using PSP at ONERA, 39th AIAA Aerospace Sciences Meeting& Exhibit, Reno (2001) AIAA 2001–0555
4.93 Y. Shimbo, R. D. Mehta, B. J. Cantwell: Vortical flow field investigation using the pressure sensitive paint technique at low speed, 35th AIAA Aerospace Science Meeting, Reno (1997) AIAA 97–0388
4.94 Y. Shimbo, N. Komatsu, K. Asai: Pressure sensitive paint application at large production wind tunnels, 22nd International Congress of Aeronautical Science, Harrogate (2000) ICAS2000–3.3.3
4.95 C. Y. Huang, H. Sakaue, J. W. Gregory, J. P. Sullivan: Molecular sensors for MEMS, 40th Aerospace Sciences Meeting & Exhibit, Reno (2002) AIAA2002–0256
4.96 C. Y Huang, J. P Sullivan: Flow visualization and pressure measurement in micronozzles, 11th Int. Symp. Flow Visualization, Univ. of Notre Dome (2004)
4.97 A. Davies, D. Bedwell, M. Dunleavy, N. Brownjohn: Pressure sensitive paint limitations and solutions, Proc. 17th International Congress on Instrumentation in Aerospace Simulation Facilities, Pacific Grove (1997) pp.11–21
4.98 M. Hamner, B. Campbell, T. Liu, J. P Sullivan: A scanning laser system for temperature and pressure sensitive paint, AIAA J. (1994) 94–0728
4.99 V.O. Stern, M. Volmer: Über die Abklingungszeit der Fluoreszenz, Phys. Z. **20**, 183 (1919), in German
4.100 J.I. Peterson, R.V. Fitzgerald: Rev. Sci. Instrum. **51**, 670 (1980)
4.101 M.M. Ardasheva, L.B. Nevskii, G.E. Pervushin: Measurement of pressure distribution by means of indicator coatings, J. Appl. Mech. Techn. Phys. **2**, 469–474 (1985)
4.102 M. Brenci: Fibre optic optrodes for chemical sensing, Proc. Opt. Fibre Sensors (1993)
4.103 M. E. Sellers, I. A. Brill: Demonstration test of pressure sensitive paint in the AEDC 16ft transonic wind tunnel, AIAA paper 94–2481, I8th AIAA Ground Testing Conference (1994)
4.104 W. Holmes: The relevance of pressure sensitive paint to aerodynamic research, J. Fluoresc. **3**(3), 179–183 (1994)
4.105 B. Carroll, M. Morris: Step response of pressure sensitive paint, AIAA J. **34**(3), 521–526 (1996)
4.106 The Boeing Aircraft Company, St Louis (2006)
4.107 J. W. Holmes: Pressure sensitive paint measurements in the DRA 8 ft × 8 ft high speed wind tunnel (GARTEUR Version) DRA/AS/HWA/TR95051/1, October (1995)
4.108 S. D. Schwab, R. M. Levy: Pressure sensitive paint formulations and methods, US Patent 5,359,887, Nov. 1 (1994)
4.109 G. M. Zharkova, A. I. Maksinov, A. A. Pavlov, V. M. Khachaturyan: Pressure visualization on aerodynamic surface by the method of luminescent coating, Proc. 6th Int. Symp. on Flow Visualization Yokohama (Springer, Heidelberg 1992)
4.110 F. Rodriguez: *Principles of Polymer Systems*, 2nd edn. (McGraw-Hill, New York 1987)
4.111 H. Sakaue, J.P. Sullivan: Time response of anodized aluminum pressure-sensitive paint, AIAA J. **39**, 1944–1949 (2001)
4.112 N.A. Winslow, B.F. Carroll, A.J. Kurdila: Model development and analysis of the dynamics of pressure-sensitive paints, AIAA J. **39**, 660–666 (2001)
4.113 R. H. Engler: Pressure sensitive paints in quantitative wind tunnel studies, Proc. 11th Int. Symp. Flow Visualization, University of Notre Dame, South Bend (2004)
4.114 T. Liu, J.P. Sullivan: *Pressure and Temperature Sensitive Paint* (Springer, Heidelberg 2004)
4.115 R. H Engler: PSP and TSP for different Wind Tunnels and Flow Facilities, The 8th International Symposyium on Fluid Control, Measurement and Vizualization, Chengdu (2005)
4.116 K.R. Schanze, B.F. Carroll, S. Korotkevitch, M. Morris: Temperature dependence of pressure sensitive paints, AIAA J. **35**(2), 306–310 (1997)
4.117 J. Kavandi: Luminescent barometry in wind tunnels, Rev. Sci. Instrum. **61**, 11 (1990)
4.118 B. G. McLachlan, J. H. Bell: Flight testing of a luminescent surface pressure sensor, NASA Tech. Memorandum 103970 (1992)
4.119 U. Henne: Application if the PSP technique in low speed range wind tunnels, STAB Workshop, Göttingen (2005)
4.120 C. Parker: *Photoluminescence of Solutions* (Elsevier, Amsterdam 1968), Chapter 1C
4.121 N.J. Turro: *Modern Molecular Photochemistry* (Univ. Science Books, New York 1991)
4.122 O. Wolfbeis: Fibre-optical fluor sensors in analytical and clinical chemistry, Chem. Anal. **77**, 129 (1988)
4.123 A. Vollan, L. Alati: A new optical pressure measurement system, 14th ICIASF Congress (1991) p. 3
4.124 B. Ranby, J.F. Rabek: *Singlet Oxygen: Reactions with Organic Compounds and Polymers* (Wiley, New York 1978)
4.125 A. Juris, V. Balzani, F. Barigelld: Ru (II)polypyridine complexes: Photophysics, photochemistry, electrochemistry, and chemo luminescence, Coord. Chem. Rev. **84**, 85277 (1988)
4.126 F. Lythe: Die luminescence of Tris (Bipyridyl) ruthenium (11) chloride, J. Am. Chem. Soc. **91**(2), 131–137 (1969)

4.127 S. Pauly: Permeability and diffusion data. In: *Polymer Handbook*, ed. by J. Brandrup, E.H. Immergut (Wiley Interscience, New York 1989)

4.128 J.R. Welty: *Engineering Heat Transfer* (Whiley, New York 1974) pp. 102–114

4.129 A. Bukov, V. Pesetsky: Optical surface pressure measurements: Accuracy and application field evaluation, Proc. AGARD CP535, Brussels, 73rd Fluid Dynamics Panel, October (1993) Paper 24

4.130 E.U. Condon, H. Odishaw: *Handbook of Physics* (McGraw Hill, New York 1958)

4.131 B. Carroll, A. Winslow, J. Abbitt, K. Schanz, M. Morris: Pressure sensitive paint application to a sinusoidal pressure fluctuation, IEEE ICIASF Record Wright–Patterson AFB (1995) 35/1–35/6

4.132 R. H. Engler: Further developments of pressure sensitive paints (OPMS) for non flat models in steady transonic flow and unsteady conditions IEEE ICIASF Record Wright–Patterson AFB (1995) 33/1–33/8

4.133 V. Borovoy, A. Bukov, V. Mosharov, et al.: Pressure sensitive paint in shock wind tunnel, IEEE ICIASF Record Wright–Patterson AFB (1995) 34/1–34/4

4.134 S. F. Hoemer: Fluid–dynamic drag, Library on Congress Catalog Card Number 64–19666 (1965) chapters 2 and 5

4.135 U. Fey, R. H. Engler Y. Egami, Y. Iijima, K. Asai, U. Jansen, J.Quest: Transition detection by temperature sensitive paint at cryogenic temperatures in the European Transonic Wind Tunnel (ETW), ICIASF'03 Record, Göttingen (2003) pp. 77–88

4.136 S. D. Torgerson, T. Liu, J. P. Sullivan: Use of pressure sensitive paints in low speed flows, AIAA–96–2184,19 AIAA Advanced Measurement and Ground Testing Technology Conference (1996)

4.137 K. Jules, M. Carbonaro, S. Zemsch: Application of pressure sensitive paints in hypersonic flows, NASA Tech. Memorandum 106824, February (1995)

4.138 J. W. Grate, M. H. Abrahams: Solubility properties of siloxane polymers for chemical sensors, Pacific Northwest Fibre Optic Sensors Workshop 3–4, SPIE 2574:71–77 (1995)

4.139 K. Goswami, S. Klainer: Fibre optic chemical sensor for the measurement of partial pressure of oxygen, SPIE **990** (1988)

4.140 M. J. Morris, et al.: Aerodynamic applications of pressure sensitive paint, AIAA J. (1992) paper 92–0264

4.141 J. F. Donovan, et al.: Data analysis techniques for pressure–and temperature–sensitive paint, AIAA J. (1993) paper 93–0176

4.142 C. Klein, R. H. Engler: First results using the new DLR PSP system–Intensity and lifetime measurements, 43.1–43.9 Proc. CEAS Wind Tunnels Wind Tunnel Test Tech. Conf. Cambridge (1997)

4.143 A. Draeijer, R. Sanders: Fluorescence lifetime imaging: a new tool in confocal microscopy. In: *Handbook of Confocal Microscopy* (Plenum, New York 1995)

4.144 A. G. Davies: Recent developments in pressure sensitive paint measurements using the BAe system, 28.1–28.11 Proc. CEAS Wind Tunnels Wind Tunnel Test Techn. Conf. Cambridge (1997)

4.145 S. P. Burns, I. P. Sullivan: The use of pressure sensitive paints on rotating machinery, IEEE ICIASF Record Wright –Patterson AFB (1995) 32.1–32.14

4.146 J. W. Holmes: Analysis of radiometric, lifetime and fluorescent lifetime imaging, J. Roy. Aeronaut. Soc. (1998) Paper 2306

4.147 R. C. Crites: Pressure sensitive paint technique, Measurement Techniques Lecture Series 1993–05, von Karman Institute for Fluid Dynamics (1993)

4.148 S. W. Houck, R. G. Hepp, M. I. Morris, M. E. Benne: Pressure sensitive paint flight test, IEEE Aerospace Applications Conf., Aspen Co 4:241–252 (1996)

4.149 C. A. Fuentes, J. D. Abbitt: Development of a film–based pressure sensitive paint technique, AIAA 96–2933, 32nd AIAA/ASME/SAE/ASEE Joint propulsion conference, Lake Buena Vista, FL (1996)

4.150 R. D. La Belle, S. D. Garvey: Introduction to high performance CCD cameras, IEEE ICIASP Record Wright–Patterson AFB (1995)

4.151 R. H. Engler, U. Fey, U. Henne, C. Klein, W. E. Sachs: Pressure sensitive paints and temperature sensitive paints in quantitative wind tunnel studies, J. Visualization (2004) paper 04–053

4.152 N. Brown, M. E. Benne, M. E. Kammeeyer: Factors influencing camera selection for the boing pressure sensitive paint system, Proc. 42nd AIAA Aerospace Sciences Meeting and Exhibit (2004) AIAA–2004–294

4.153 S. S. Bowen: Comparison of motion estimators for an intensity variant image sequence, SPIE Image and Video Processing H 2182 (1994)

4.154 W.M. Ruyten: Self–illumination calibration technique for luminescent paint measurements, Rev. Sci. Instrum. **68**(7), 3452–3457 (1997)

4.155 Y. Mebarki: Peintures sensibles a lapression: Application en soufflerie aerodynamique, Thesis (University of Lille, Lille 1997)

4.156 M. J. Morris, J. F. Donovan: Application of pressure–and temperature sensitive paints in high speed flows, AIAA J. 94–2231, 25th AIAA Fluid Dynamics Conference (1994)

4.157 B.G. McLachlan, J.H. Bell, H. Park, et al.: Pressure–sensitive paint measurements on a supersonic high–sweep oblique wing model, J. Aircraft **32**(2), 470–483 (1995)

4.158 J. Holmes: Analysis of radiometric, lifetime and fluorescence lifetime imaging, Aeronautical J. **2306**, 189–194 (1998)

4.159 L. Goss, D. Trump, B. Sarka, L. Lydick, W. Baker: Multi-dimensional time-resolved pressure-sensitive-paint techniques: A numerical and experimental comparison (2000) AIAA 2000–0832

4.160 L. Coyle, M. Gouterman: Correcting Lifetime Measurements for Temperarure, Sens. Actuat. B **61**, 92–99 (1999)

4.161 J. Hradil, C. Davis, C. Mongey, C. McDonagh, B.D. MacCraith: Temperature-corrected pressure-sensitive paint measurements using a single camera and a dual-lifetime approach, Meas. Sci. Technol. **13**, 1552–1557 (2002)

4.162 K. Mitsuo, Y. Egami, H. Suzuki, H. Mizushima, K. Asai: Development of lifetime imaging system for pressure-sensitive paint (2002) AIAA 2002–2909

4.163 K. Mitsuo, K. Asai, A. Takahashi, H. Mizushima: Advanced lifetime PSP imaging system for simultaneous pressure and temperature measurement (2004) AIAA 2004–2188

4.164 A. Watkins, J. Jordan, B. Leighty, J. Ingram, D. Ogelsby: Development of next generation lifetime PSP imaging system, Proc. 20th Int. Congr. Instrum. Aerospace Simulation Facilities, Gottingen (2003) pp. 372–377

4.165 R. H. Engler: PSP/Acoustic circulation method for surface pressure and flow field investigation around a delta wing, Proc. 21th Int. Congr. Instrum. Aerospace Simulation Facilities, Sendai (2005)

4.166 B. Schulze. C. Klein: Light emitting surfaces of wind tunnel models for excitation of pressure sensitive paint, Proc. 21th Int. Congr. Instrum. Aerospace Simulation Facilities, Sendai (2005)

4.167 W. Ruyten: Assimilation of physical chemistry models for lifetime analysis of pressure-sensitive paint (2004) AIAA 2004–0880

4.168 W. Ruyten, M. Sellers: Lifetime analysis of pressure-sensitive paint PtTFPP in FIB' (2004) AIAA (2004)–0881

4.169 W. Ruyten: Optimization of three-gate lifetime pressure-temperature-sensitive paint measurements (2004) AIAA 2004–2190

4.170 L. Goss, G. Jones, J. Crafton, S. Fonov: Temperature compensation in time-resolved pressure measurements, Proc. 11th Int. Symp. Flow Visualization, University of Notre Dame (2004)

4.171 E. Puklin, B. Carlson, S. Gouin, C. Costin, E. Green, S. Ponomarev, H. Tanjii, M. Gouterman: Ideality of Pressure Sensitive Paint. I. Platinum Tetra(pentafluorophenyl)porphine in Fluoroacrylic Polymer, J. Appl. Polym. Sci. **77**(8), 2795–2804 (2002)

4.172 R. H Engler: DLR intensity and lifetime systems, PSP Workshop Pressure Sensitive Paint Workshop, NASA Langley Research Center (2000)

4.173 D. Gebbie, M. Reeder, C. Tyler, V. Fonov, J. Crafton: PSP-based experimental investigation of a blended wing body aircraft (2005) AIAA 2005–4719

4.174 J.H. Bell, et al.: Surface Pressure MeasurementsUsing Luminescence Coatings, Annu. Rev. Fluid Mech. **33**, 155–206 (2001)

4.175 S. Fonov, R. H. Engler, C. Klein, S. Mihailov, V. Mosharov, V. Kulesh, V. Radchenko, E. Schairer: Investigations of the pressure fields on the oscillating wings by pressure sensitive paint, Proc. 11th DGLR-Fach-Symposium der AG STAB vom 10–12 Nov. Technischen Universität, Berlin (1998)

4.176 M. Sajben: Uncertainty estimates for pressure sensitive paint measurements, AIAA J. **31**(II), 2105–2110 (1993)

4.177 M. J. Morris: Use of pressure–sensitive paint in low–speed flows, IEEE ICIASF Record Wright–Patterson AFB (1995)

4.178 O.C. Brown, R.D. Mehta, B. T. Cantwell: Low–speed flow studies using the pressure sensitive paint technique, 81th AGARD conference, Seattle (1997)

4.179 N. G. Verhaagen, L. N. Jenkins, S. B. Kern, A. E. Washburn: A study of the vortex flow, over a 76/40 deg double delta wing, NASA Contractor Report 195032, ICASE Report 95–5 (1995)

4.180 W. Ruyten, C. Fisher: On the effects of reflected light in luminescent paint measurements, 38th Aerospace Sciences Meeting and Exhibit, AIAA-2000–0833 (2000)

4.181 V. E. Mosharov, V. N. Radchenko, S. D. Fonov: Luminescent pressure sensors in aerodynamic experiments, published privately. Contact S. D. Fonov, TsAGI, Zhukovsky, 140160, Moscow reg., USSR or M. Osin, RUKAR, Russia (1994)

4.182 O. Trinks: Entwicklung und Einsatz einer Fluoreszenz-Lebensdauer-Methode zur Bestimmung instationärer Strömungsvorgänge an Verdichterschaufeln unter Verwendung druckempfindlicher Beschichtungen, Dissertation, Universität Göttingen (2000)

4.183 Fonov, L. Goss, J. Jones, V. Crafton, M. Fonov: New method for surface pressure measurements, 43rd AIAA Aerospace Science Meeting, Reno (2005) AIAA-2005–1029

4.184 R. H. Engler: Pressure sensitive paint in quantitative wind tunnel studies CEAS/KATnet Conference on Key Aerodynamic Technologies, Hilton Bremen (2005)

4.185 C. Klein, W. E. Sachs, U. Henne, R. H. Engler, A. Wiedemann, R. Konrath: International vortex flow experiment 2 (VFE-2), Experimental Pressure Distribution on the 65° Delta Wing Configuration using PSP, (Paper in preparation for the 44th AIAA Congress, Reno (2006))

4.186 M. Kurita, K. Nakakita, K. Mitsuo, S. Watanabe: Data processing of pressure-sensitive paint for industrial wind tunnel testing, 24th AIAA Aerodynamic Measurement Technology and Ground Testing Conference, Portland (2004) Paper 2004–2189

4.187 M. Benne, R. Kammeyer, J. Donovan, M. Rueger, J. Harris, D. Morgenroth, E. Green: General strategy for the development of an improved pressure–sensitive paint system, 2nd AIAA Aerodynamic Measurement Technology and Ground Test Conference, St. Louis (2002) AIAA 2002–2906